Structure−Performance Correlation Guided Applications of Covalent Organic Frameworks

Hou Wang[1,2,3,*], *Yi Yang*[1,2], *Xingzhong Yuan*[1,2,*], *Wei Liang Teo*[3], *Yan Wu*[4], *Lin Tang*[1,2], *and Yanli Zhao*[3,*]

[1] College of Environmental Science and Engineering, Hunan University, Changsha 410082, P. R. China

[2] Key Laboratory of Environment Biology and Pollution Control, Hunan University, Ministry of Education, Changsha 410082, P. R. China

[3] Division of Chemistry and Biological Chemistry, School of Physical and Mathematical Sciences, Nanyang Technological University, 21 Nanyang Link, Singapore 637371, Singapore

[4] College of Resources and Environment, Hunan Agricultural University, Changsha 410128, P. R. China

*E-mail: wangh@hnu.edu.cn; yxz@hnu.edu.cn; zhaoyanli@ntu.edu.sg

Abstract: Pre-designed structures and tailor-made functions make covalent organic frameworks (COFs) quickly become promising reticular platforms for multidisciplinary fields. Despite the overarching success, controllable and large-scale synthesis of COFs is still a huge challenge. Moreover, the relationship between the structure and performance of COFs in various fields has not been well understood, seriously limiting their practical applications. In this review, we provide an insightful and fundamental understanding of COFs from structural perspectives, and correlate them with eventual performance in practical applications. By summarizing both the top-down and bottom-up approaches, we address how typical issues, such as the size, morphology, dispersity and stability of COFs, are resolved, which should be crucial for their function-oriented and large-scale production. Structural and physicochemical properties, such as pores, ligands, stacking, linkages, functional group, morphology, crystallinity, dimensionality and wetting, are also discussed in relation to various functions. In addition, in-depth discussions regarding the correlations between structural characteristics of COFs and their performance in catalysis, energy storage, gas/liquid adsorption and membrane

separation are presented. Finally, perspectives for the future direction of this field are proposed, to provide useful guidance for the function-oriented design and scalable production of COFs to meet the practical requirements of applications.

Keywords: covalent organic frameworks, large-scale synthesis, performance, practical applications, structure design

Introduction

Porous materials are increasingly important in technology and applications. Although the quantity of novel and advanced porous functional materials has been exploded in recent years, constructing persistent porous structures connected by covalent bonds is still a formidable task [1–3]. The multifunctionality of the framework chemistry can achieve interesting properties, such as utilizing the internal space by contrivable and various skeleton, as well as controlling molecular level substances to decorate pore environments in the framework [4,5]. Covalent organic frameworks (COFs) are two-dimensional (2D) or three-dimensional (3D) crystalline porous organic polymers, constructed by connecting structural units via covalent bonds [6,7]. Different from amorphous porous organic polymer, COFs possess many favorable features, such as pre-designable structure, tailorable functionality, structural diversity, periodic ordered domain, adjustable crystal structure, low density, good thermal stability, high surface area, and permanent porosity [8–11]. Especially, the ordered structures in crystalline COFs possess favorable conjugation length, which is beneficial for the alignment of the π system and charge transport. It also endows COF materials with large surface area, higher porosity and more exposed active sites, while amorphous porous organic polymers often have relatively shorter conjugation length and lower surface area [12–25].

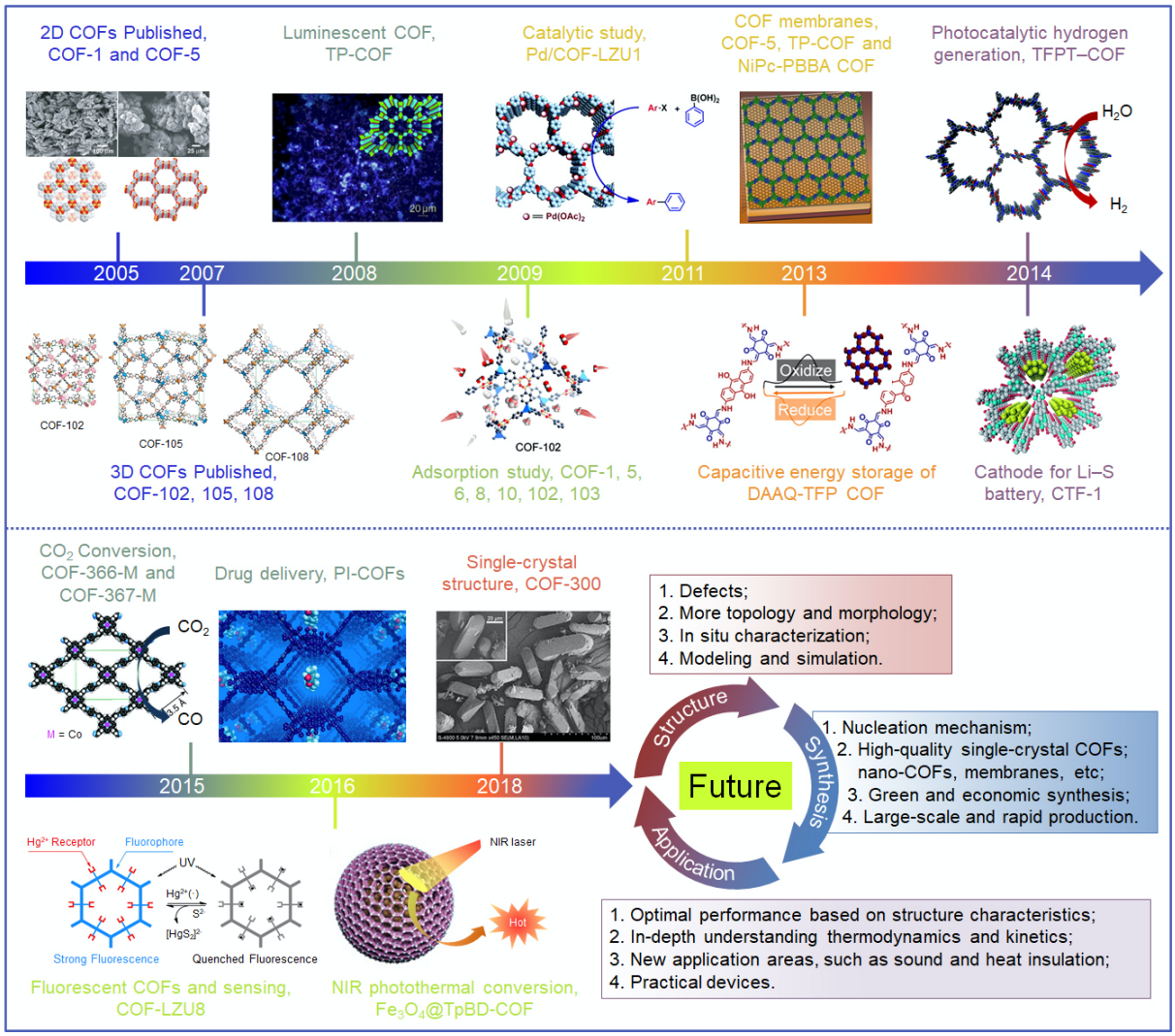

FIGURE 1. A timeline for the major advances of COFs and their promising developments. Reproduced with permission [7,13–25]. Copyright 2008 and 2016, John Wiley and Sons; Copyright 2014, Royal Society of Chemistry; Copyright 2009, 2011, 2013, 2015, and 2016, American Chemical Society; Copyright 2005, 2007, 2011, 2015, and 2018, American Association for the Advancement of Science.

Pore diameter of COFs' channels is usually between several angstroms [26,27] and a few nanometers [28,29], which can be precisely adjusted at an atomic level by changing the size of the precursors. The shape of the pores can also be controlled by choosing the desired symmetry [30,31]. The growth of polymer backbone and geometry matching between the monomers are achieved via the guidance of topology design [32,33]. Intramolecular hydrogen bond can further induce conformational switching of molecular linkages, which can

effectively regulate the topology of COFs further [34]. Properties in layered COFs, including chemical stability, crystallinity and porosity, are largely influenced by the way adjacent sheets are stacked [35]. Reactivity of COF materials is due to either the network topology and physical-chemical functions of organic framework, or the restriction of spatial environment in channel and interlayer. In particular, the framework space and interface generated by pores can interact with ions, molecules, photons, or holes, leading to superior structural and functional properties [36,37]. Typically, introducing neutral, polar, and cationic sites as well as Lewis base into the pore wall of 2D COF is beneficial for proton conductivity. The proton conductivity of a COF named PA@EB-COF41 was greatly improved to 2.77×10^{-2} S cm^{-1} [38]. Aligned ethidium-biphosphate ion-pairs, formed in the cationic channel, reduce the proton dissociation energy and simultaneously serve as proton transfer sites to enhance proton conductivity. Thus, COFs have attracted considerable interests in the fields of catalysis [39–42], energy storage [43–46], adsorption [47–49] and membrane separation [50–52], since their discovery (Fig. 1).

The diversity of COFs is enriched with different compositions and geometries (Fig. 2). Up till now, COFs with multidimensions (1-dimension, 2-dimension, 3-dimension, etc.), multitudinous linkages (imine, ethylene, ketoenamine, etc.), diverse shapes (spherical, tubular, nanosheets, nanoparticles, etc.), distinct topologies (*hcb*, *hxl*, *mta*, *tth*, *dia*, *ctn*, *ffc*, *ceq*, etc.) [53] and different structures (crystallinity, π-conjugated scaffold, defects, etc.) were developed. Furthermore, different building units of COFs enables different properties and applications [54]. The valency in COFs can also be enriched through the development of large COF single crystals composed of cube (valency 8) and rod units (valency “infinity”) [55]. Within the above context, the term “structure-performance” was coined to describe artificial molecular framework that alter reactive performance through reticular chemistry. Therefore, understanding fields-focused structure-performance correlations diversify the processability and availability of COFs in the fields of catalysis, energy storage, adsorption and membrane separation.

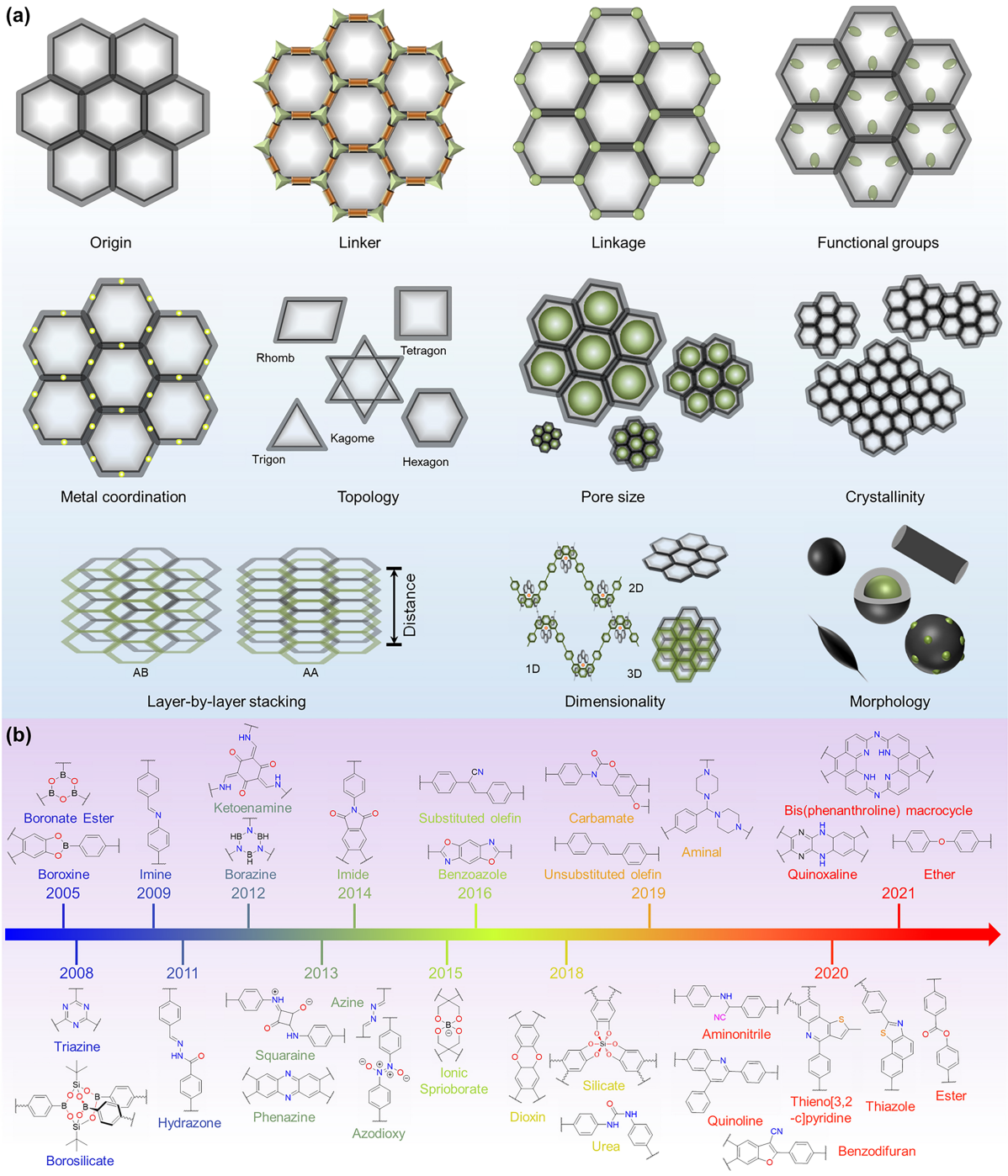

FIGURE 2. (a) Illustrative examples of different structural COFs; (b) Research progress of COFs with typical covalent linkages.

Especially, it is much more challenging for COFs to be utilized for biomedical application, due to their large size and irregular morphology. At the same time, it is difficult to process insoluble bulk COFs powders, which further inhibits progress in this research direction. However, recent progresses in synthetic methodologies manage to address such shortfalls,

with the manufacture of COFs nanoparticles and nanoflakes, utilizing bottom-up and top-down strategies. Notably, the high-quality COF films (< 75 nm) prepared through bottom-up strategy had excellent thermal conductivity (1 W m^{-1} K^{-1}) and low dielectric constant (k = 1.6) [56]. Bottom-up methods mainly involve solvothermal technique, ionothermal synthesis, in-situ surface conversion, topology-templated synthesis and interfacial preparation while top-down methods include liquid phase exfoliation and mechanical delamination. At the same time, large-scale synthetic methodologies were also developed, allowing for the exploration of processable COFs and related devices.

Although many reviews focused on the respective design, synthesis and application for COFs [57–62], little discussion about the field-focused structure-performance correlations and large-scale and/or rapid synthesis is available. This review updated typical strategies of COFs synthesis and summarized various methods for large-scale and/or rapid preparation. Through a variety of different features and mechanisms, the structure-performance correlations for catalysis, energy storage, gas/liquid adsorption and membrane separation were systematically discussed. Future opportunities and challenges were also highlighted from the perspective of chemistry, materials, and industrial application.

Influence of synthetic strategies on structures and functions

COFs are constructed via strong dynamic covalent bonds from simple building units. Dynamic processes are mainly affected by polymerization conditions, including reaction time, temperature, pressure, pH, solvent, catalyst, monomer concentration and monomers feed rate. These made the chain crystallization and propagation process very complex. Essentially, COFs undergo a nucleation-elongation process [63,64]. The key to manufacturing high-quality COFs crystals is the precise control of nucleation and growth rates, which are involved in second-order and first-order reaction dynamics, depending on monomer concentrations [65,66]. Reducing the steady-state monomer concentration can inhibit nucleation and facilitate the growth of crystallites for micron-level size [67]. Notably, defects are caused by i) covalent bonding during the growth process, ii) secondary new complex (mainly involving pentagonal defects of [C_4+ C_4] and [C_4 + C_2], heptagonal defects of [C_3+ C_3] and [C_3+ C_2]) [68], and iii) robust bonding energies rendering undue nucleation rate and

growth. These factors hinder the crystallization when monomers polymerize, and frequently bring about amorphous films featuring small crystal domains or polycrystalline powders [69,70]. Several strategies are adopted to decrease defects, such as coupling building block design and growth dynamics control [70], reducing the activity and binding energy of reversible reactions [71], and realizing growth via adding monomers to a single nucleus [68]. Conventional synthetic methods in a sealed vessel under solvothermal conditions are the most useful to optimize the crystallites via the screening procedures due to the sensitivity of COF quality. Subsequently, other methods including mechanochemical synthesis, interfacial synthesis, ionothermal synthesis, in situ on-surface conversion have been developed and demonstrated [61]. Two main strategies including bottom-up fabrication and top-down approach have been explored for the preparation of nano/microstructural COFs (Fig. 3).

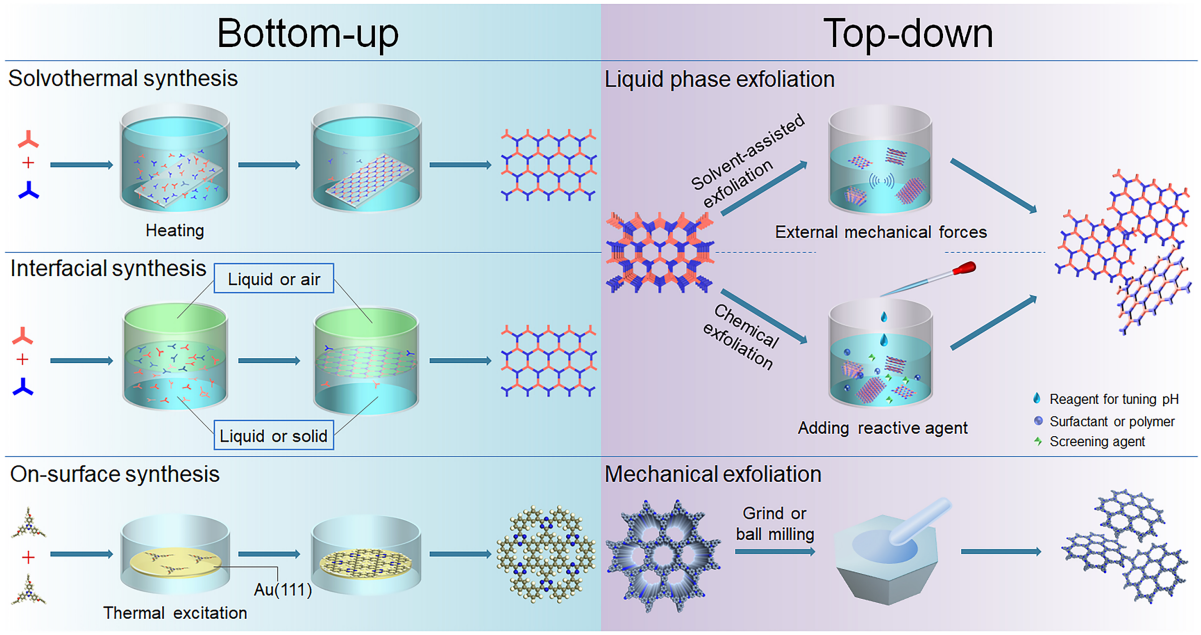

FIGURE 3. Different routes used to prepare high-quality nano/microsized COFs.

Bottom-up approach

Bottom-up strategy involves designing ordered structures linked by covalent bonds through reversible and irreversible reactions between organic blocks. This strategy can easily control the diameter, shape, and functionality of COFs [72–75]. Bottom-up strategies consist of solvothermal synthesis, ionothermal synthesis, interfacial synthesis, in situ on-surface

conversion and some new strategies, such as coordination and dynamic covalent synthesis, 2D to 3D reversible conversion of COFs and topology-templated synthesis.

Solvothermal synthesis. Solvothermal synthesis is most prominent and frequently adopted strategy for COF synthesis, where reaction mixture is heated and condensed in a closed device to form crystallized COFs [13]. Solvothermal synthesis is typically time consuming (usually 5-7 days), uses high energy, requires complicated operational steps and produces volatile organic compound. Several attempts at addressing these shortfalls are demonstrated. To shorten the reaction time of imine-linked COFs, 1,2,4-triazolium poly(ionic liquid)s (PILs) were utilized as additives [76]. Single-crystal COFs with 5 μm size were generated within 10 min. This is largely attributed to the catalytic effect of active C5-protons within poly(1,2,4-triazolium)s on forming imine linkages. Supercritically solvothermal polymerization was developed to prepare 0.2 mm single-crystal COFs within 2 to 5 min [77]. This ultrafast single-crystal polymerization benefits from the low surface tension, low viscosity, and high diffusion coefficient of supercritical fluids. To reduce synthetic costs, vinylene-linked COF-701 was synthesized using cheap acetonitrile as solvent through two consecutive reactions involving cyclotrimerization of nitriles and aldol condensation [78]. Using water as the solvent and a limited amount of acetic acid as the catalyst additive at low temperatures, the incubatory process of imine-linked COFs can avoid harmful organic solvents and high temperatures [79]. Remarkably, by using microwave heating, reaction time at 35 °C for the generation of imine-linked COFs was significantly reduced from 5 d to 5 h, as compared to conventional heating at 80 °C. This green synthetic strategy is promising for the large-scale sustainable synthesis of imine-based COFs in water.

Ionothermal synthesis. Ionothermal synthesis is the most widely used method in the synthesis of covalent triazine frameworks (CTFs) through the trimerization of nitriles in molten metal salt [80]. To reduce environmentally harmful solvents, reaction temperature (400 °C) and reaction time (40 h), an ionothermal synthesis methodology for the synthesis of polyimide-linked COFs in pure $ZnCl_2$ or eutectic salt mixtures (NaCl/KCl/$ZnCl_2$) was developed [81]. TAPB-PTCDA-COF and TAPB-PMDA-COF were fabricated within 10 hours at 300 °C in the presence of anhydrous $ZnCl_2$, with the yields of 78% and 88% respectively. The formation of intermediates (the crystalline adducts composed of $ZnCl_2$ and the

corresponding precursors), which activate the anhydride and imide rings, reduces the overall barrier of activation, enhancing the reversibility of COFs formation. Compared with solvothermal synthesis, this straightforward method does not require additional toxic solvents, base catalysts, as well as soluble precursors. However, final products usually have poor crystallinity and may cause partial carbonization due to high reaction temperature and long reaction time.

Interfacial synthesis. There are three types of interfaces, namely liquid-air interface, liquid-liquid interface and solid-vapor interface, where reaction between monomers occurs. Restricted by the limited interfacial area, COFs usually grow into thin film for these cases. The liquid/air interface was favorable to the formation of COFs films caused by the easily controlled nucleation and thicknesses [82]. For instance, simple aromatic triamines and dialdehyde structural units can be assembled to form COF monolayers at the air/water interface [83]. N-hexyl hydrophobic groups on the aromatic triamine monomers were directed perpendicular to the coating surface while all benzene rings were anchored on the interface by hydrophilic amino groups. Triamine and dialdehyde units were assembled to form strain-free imine bonds. Precursors undergo self-correction, due to the reversibility of these bonds, to form smooth and ordered 2D COF thin sheets with uniform thickness.

For completing the ordered arrangement of pores after initial polymerization, COFs films need beforehand ordered domain, which is a time-consuming procedure. During liquid-liquid interfacial polymerization (IP), film formation (24 h) usually occurs before crystallization (72 h) [84]. Reaction temperature can be raised to reduce the time taken, which could result in cracked or defective films as the fragile liquid-liquid interface was disturbed. A dilemma situation is that the longer-time reaction would induce a thicker film with large polymeric particles as diffusion becomes more extensive across the liquid-liquid interface. A fine balance is needed to obtain a suitable thin film product [85]. Remarkably, solid-vapor interfacial polymerization is an effective way to increase the reaction temperature to improve the reaction rate without disturbing with the interface significantly, thus improving the time mismatch between polymerization and crystallization during COF synthesis. It also confines the interfacial reaction, since the monomer is in a static solid phase, which lowers the thickness of the film. For example, choosing *p*-phenylenediamine (PDA) as the vapor-phase

monomer, 1,3,5-triformylphloroglucinol (TFP) as the solid-phase monomer, a single-layer COF film with thickness of 120 nm was manufactured at 150 °C in 9 h [86]. Sufficient kinetic energy from the vapor phase monomers gave rise to favorable vapor pressure and diffusion rate to accelerate the polymerization reaction and nucleation speed at the interface, which shortens the reaction time.

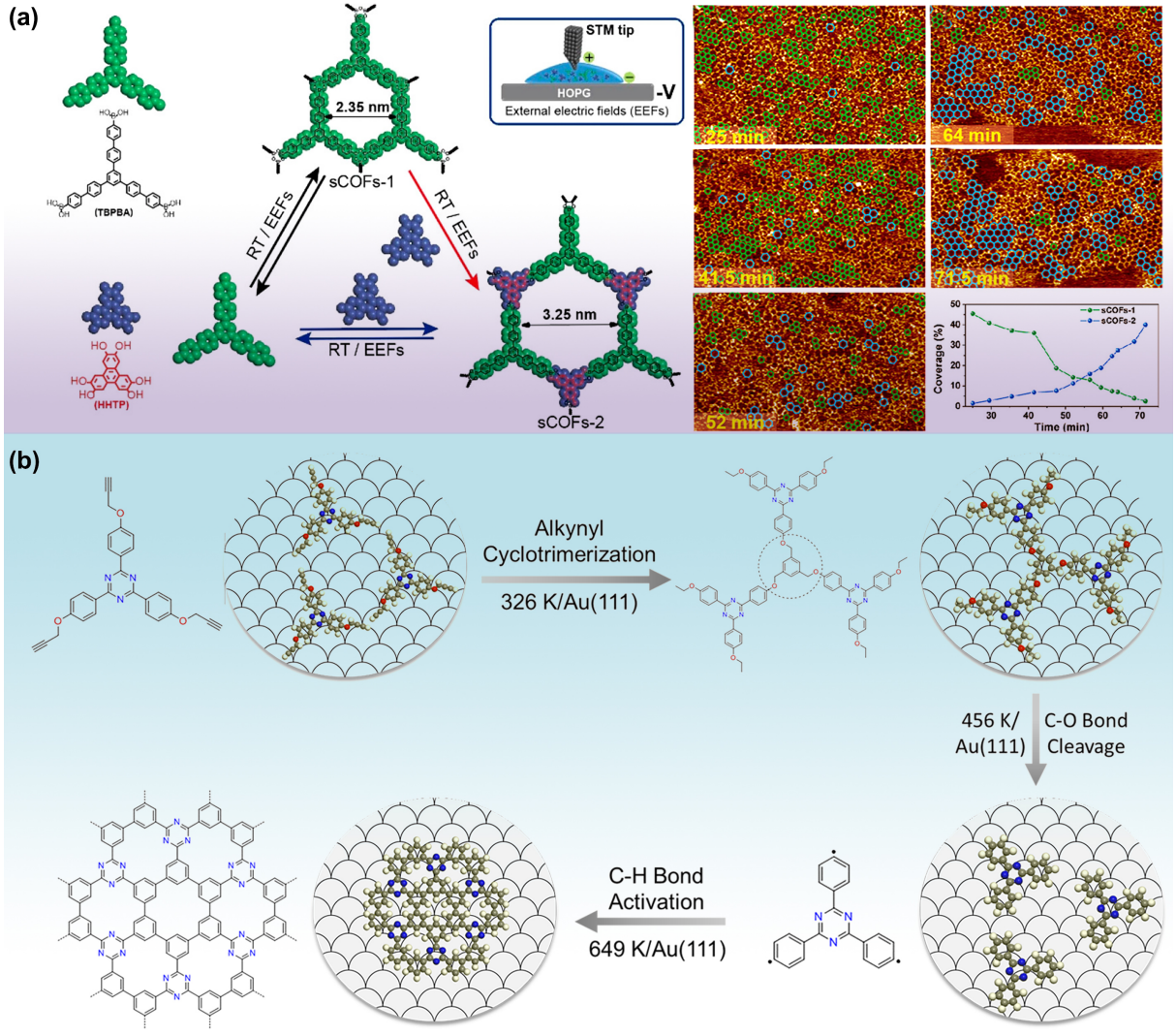

FIGURE 4. (a) Left: EEF-mediated network switching between sCOFs-1 and sCOFs-2; Right: sequential STM images exhibiting the time-dependent network switch process. Reproduced with permission [95]. Copyright 2020, American Chemical Society. (b) On-surface synthesis of t-COFs through stepwise reactions of Ph-PET on Au(111). Reproduced with permission [96]. Copyright 2020, John Wiley & Sons, Inc.

In situ on-surface conversion. Dynamic covalent chemistry (DCC) in COFs crystallization is affected by external stimuli such as temperature [87], light [88], protons [89] and metal ions [90]. Post-synthetic modification of the initially formed crystalline COFs generates new COFs, also known as COF-to-COF conversions [91–93]. In the course of unclear conversion, switching the dynamic network to single-layered COFs (sCOF) on the surface can reduce the dimensionality of the problem [94]. The *in-situ* COF linkage conversion has been visually observed from boroxine-linkage to boronate ester-linkage by triggering the catalytic reaction between tris(4-biphenylboronic acid)benzene and hexahydroxytriphenylene, using an oriented external electric field which can promote bond cleavage and formation, on a highly oriented pyrolytic graphite (HOPG) surface (Fig. 4a) [95]. Monitoring constitutional variation process is beneficial to gain insight into the synthesis process of COFs. Well-defined graphene-like single-layer COFs with triazine rings (t-COFs) have also been manufactured on Au(111) [96]. By triggering different stepwise on-surface reactions, such as cyclotrimerization of alkynyl, cleavage of C–O bond, and activation of C–H bond, *t*-COF was fabricated via thermal excitation at different stages (Fig. 4b). Also, Au(111) substrate acts as a catalyst to promote these reactions by reducing their respective reaction energy barrier. Furthermore, investigating chirality within on-surface syntheses also improves the fabrication technique of chiral covalent material with atomic precision [97,98]. Designing prochiral precursors with distinct side chains allows for the steric hindrance to surface synthesis.

New synthesis strategies. Compared with the limitations of conventional synthesis strategies in energy consumption, toxic organic solvents, and low yields, developing new synthesis methods is necessary to increase the structures' stability and diversity, as well as enrich the topology.

(1) Coordination and dynamic covalent synthesis. Combining DCC and coordination chemistry is a convenient strategy to assemble complicated compounds using simple building blocks. Several COFs with captivating topologies were synthesized by virtue of this protocol [99]. There is still a lack of efficient chemical methods to integrate covalently linked structures into crystal skeletons. Different chemical pathways were proposed for assembling 3D woven COFs (WCOF-cu, diamondoid topologies with 3-fold interpenetration) or 1D metallo-COFs (mCOFs-cu) via using Cu^{I} phenanthroline complexes as the starting units, in

the presence/absence of ligand exchange [100]. Tuning the coordination forms of metal node was capable of affecting ligand exchange. Different starting units have a competitive relationship with Cu^{I}. It rendered the composite structures with a character of dynamic equilibrium. Metal coordination and dynamic covalent bond formation were shown to have a synergistic effect during the preparation of COFs. The use of ligand exchange can control the direction of COFs growth, resulting in either 1D or 3D products.

(2) 2D to 3D reversible conversion. Cross-linking polymers converts linear or slightly branched macromolecules into 3D network structures, thereby affecting the stability, mechanical strength, electronic and optical properties of the resulting products [101,102]. A typical case of an ordered and reversible conversion of 2D to 3D COF was that poly(arylenevinylene) COFs (P^2PV and P^2NV COFs) can be converted into 3D cyclobutane COFs (P^3PcB and P^3NcB COFs) under irradiation in non-polar solvent while maintaining their crystallinity [102]. Because [2 + 2] cycloaddition reaction occurred due to light irradiation, allowing P^2PV and P^2NV COF sheets to cross-link. This process brought about changes in the structures, mechanical properties, and electrical characteristics of the materials due to the change of crystal lattices, surface areas, pore size and shape, π-electron conjugations and energy gap.

(3) Topology-templated synthesis. Through topology-guided polymerization, the growths of ordered 2D or 3D chains can be triggered via monomers with matching geometries to promote nucleation and subsequent formation of crystalline COFs [103,104]. It is necessary to screen for reaction conditions to initiate nucleation, as well as to balance the extent of crystallization and polymerization. Very recently, imine-linked skeletons with different topologies, including tetragonal, hexagonal, and kagome, were selected as templates to synthesize crystalline sp^2c-COF [105]. The building blocks were directed by templates via π interactions, triggering C=C bonds formation. sp^2 carbon chains grew along the (001) facets of templates, resulting in nucleation and the fabrication of sp^2c-COF. It is worth noting that monomer geometries need to match the template topology. Also, similar channel sizes between template and target COFs are required, for enhanced π interactions. Overall, topology-templated synthesis renders COFs with tailor-made topologies and apertures. It is a

general method to obtain COFs that cannot be synthesized directly but suffers from long preparation time and requires an additional template removal step.

Notably, the bottom-up approach is a good way to synthesize special morphology of COFs, such as hollow, core-shell, and fiber morphology [106–108]. However, fast reaction rate and diffusion lead to rapid self-coagulation of initial framework products, which inhibits growth on the surface of inoculating seeds, resulting in irregular morphology [109]. The mechanism exploration of the synthesis process is relatively complicated. Especially, hollow multishelled COFs have not been synthesized so far, and a versatile method for synthesizing COFs with hollow multishelled structures is expected to be developed.

Top-down approach

Weak interactions involving hydrogen bonding, van der Waals forces, π-π interaction, etc. between the layers of bulk COFs make exfoliation into nanosheets possible without specific interface or substrate [110,111]. Generally, using external or internal forces enable the production of single/multilayered sheets. In this section, we summarized two methods including liquid phase exfoliations and mechanical exfoliations.

Liquid phase exfoliation. (1) Organic solvent-assisted exfoliation. Using external mechanical forces (e.g., ultrasound and ultrasonic bombardment), the layered bulk COFs can be exfoliated into ultrathin 2D nanosheets in the liquid phase [112]. The use of sonication introduces microbubbles into solution. When these microbubbles burst, micro-jet and shock waves with strong tensile stress are generated, exfoliating bulk material into a few layered COF sheets. Solvent choice significantly affects the exfoliation process. An appropriate solvent system for a particular type of framework can not only promote the exfoliated capacity, but also prevent the aggregation of exfoliated nanosheets [113]. After exfoliating the hydrazone-linked COF-43 nanosheet [114], the crystallinity decreased when COF-43 powder was submerged in dioxane, H_2O or dimethylformamide (DMF) compared to tetrahydrofuran (THF), $CHCl_3$ or MeOH. The introduction of flexible building units weakens the interlayer π-π interactions and makes them easier to exfoliate into nanosheets. By using two non-planar building units with C_{3v} macromolecular symmetry as building blocks, a layered [3+3] imine-linked TPA-COF was obtained and successfully peeled into ultrathin nanosheets with

ordered pore channels [112]. Recently, Burke et al. proposed the preparation of crystalline COF films with tunable thickness of ranging from 50 nm to 20 μm through acid exfoliation [115]. This approach mainly includes: i) protonating 2D imine-linked BND-TFB COF by adding excess trifluoroacetic acid; ii) exfoliating bulk BND-TFB COF into thin sheets due to electrostatic repulsion between adjacent COF layers; iii) depositing crystalline COF films on the silicon wafer; and iv) utilizing reagent alcohol to deprotonate for obtaining neutral imine-linked COF films. Notably, the films could be separated from the substrate to form robust and freestanding COF films. This strategy provides strong inspiration for large-scale production.

(2) Aqueous exfoliation. To avoid re-stacking and aggregation, surface tensions of water are reduced by the addition of polymer or water-soluble surfactant, to render stable COFs thin sheets [116,117]. APTES-COF-1 was assembled with monofunctional curcumin derivative modified by polyethylene glycol [118]. The quasi-micelle structure (surfactant and oil phase for PEGCCM and APTES-COF-1, respectively) increased the repulsive force between the layers, thereby promoting the exfoliation. It was also found that the interlaminar force of imine-linked TAPB-PDA-COF can be tuned by changing the solution pH, resulting in the production of a large amount of exfoliated few/single-layer TAPB-PDA-COF [119]. The C=N linkages are polarized to produce negatively charged nitrogen and positively charged carbon [120], which cause interlayer charge repulsion. In pH < 2.5, the stronger turbostratic effect was exhibited, causing the exfoliation of 2D structure with favorable dispersion.

(3) Reversible exfoliation and re-stacking. Reversibility of interlayer shifting process was determined by interlayer strengths of COFs [121]. Exfoliation is uncontrollable during the manufacturing of 2D COF nanosheets. COFs with weaker interlayer interactions, due to larger pore sizes, unsubstituted linear blocks and lower π-conjugation, are likely to undergo irreversible structural destruction because of solvation effects. Conversely, COFs with smaller pore sizes, containing structural substituents and larger π-conjugation possessed stronger π-π interactions and London dispersion forces, rendering excellent crystallinity as well as reversibility of COFs during the interlayer shifting process [121].

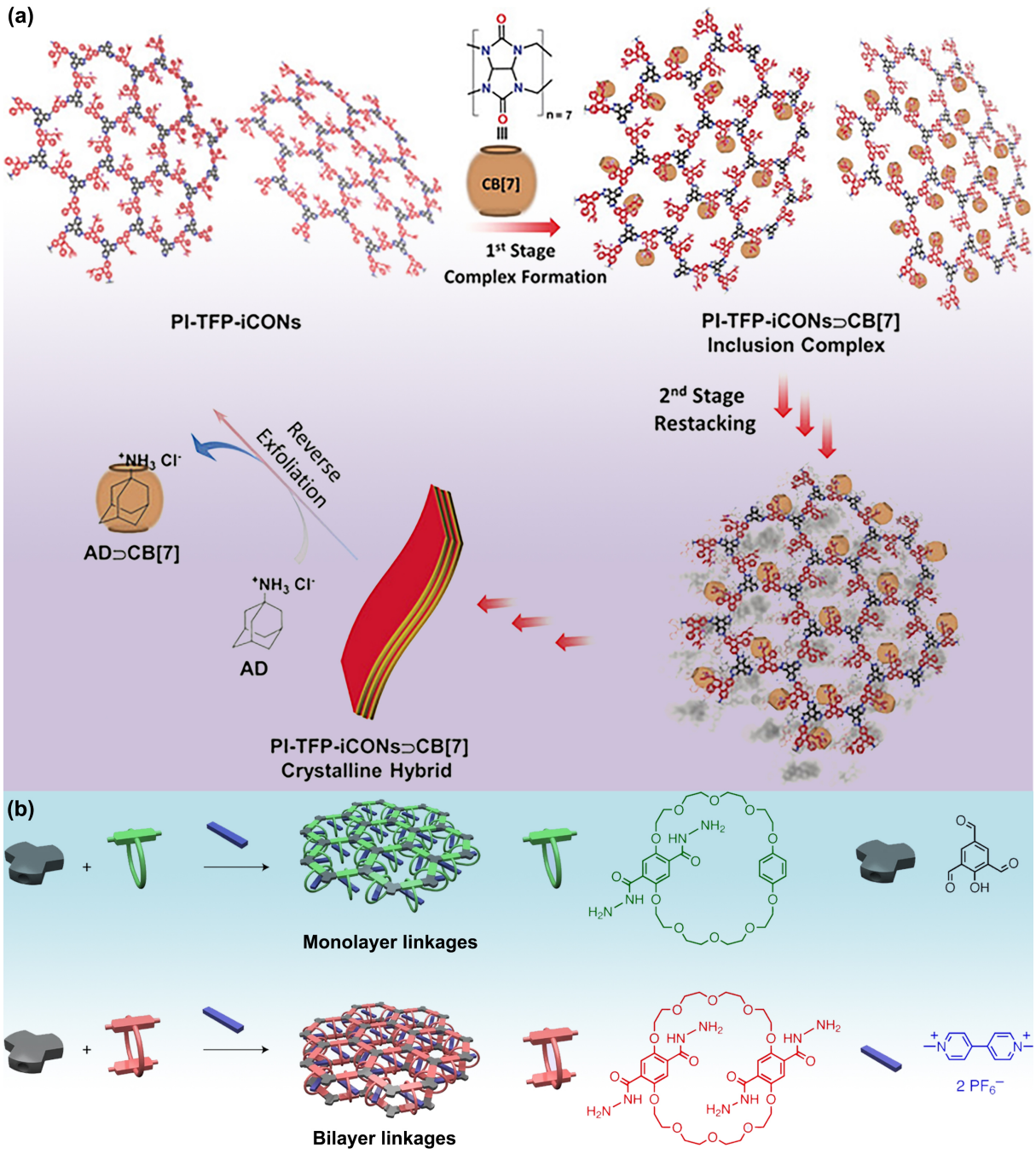

FIGURE 5. (a) Reverse exfoliation and re-stacking of PI-TFPiCONs. Reproduced with permission [125]. Copyright 2020, John Wiley & Sons, Inc. (b) Construction of 2D COFs with targeted layer numbers via mechanical bonding. Reproduced with permission [126]. Copyright 2020, Nature Publishing Group.

An equally important factor is the reversibility of the available surface charge on COFs, making controlled exfoliation, reversible stripping, and re-stacking difficult to achieve. COFs with inherent ionic charge (iCOFs) were automatically exfoliated into few layered ionic

covalent organic nanosheets (iCONs), and which can be readily restacked using double-stranded DNA [122]. The host-guest interaction is driven by molecular recognition to achieve reversible exfoliation and re-stacking via control of the available surface area and charges. COFs with ionic side chains may promote self-exfoliation, and restack by recombination with cucurbit[7]uril (CB[7]) [123,124]. Propidium iodide (PI)-based iCOFs (PI-TFP) can self-exfoliates to form an ultra-thin 2D PI-TFP-iCONs [125]. Dispersible iCONs formed PI-TFP-iCONs⊃CB[7] inclusion complexes in the presence of CB[7], which effectively masked surface charges, thus allowing PI-TFP-iCONs⊃CB was come close to each other and restacked into crystalline hybrids. The presence of competitive guest 1-adamantyl-amine hydrochloride (AD) could replace CB[7] in iCON to generate a more stable AD⊃CB[7] inclusion complex. iCON can then restore the ionic head group and increase the repulsive surface charge, which leads to the exfoliation of PI-TFP-iCON, thereby regenerating ultra-thin 2D PI-TFP-iCONs (Fig. 5a).

(4) Precise exfoliation of mono- and bi-layer COFs. Mechanically interlocked molecular architecture (e.g., pseudorotaxane) was used to exfoliate layered COFs (RCOF) [126]. The number of layers of the exfoliated COFs can be controlled precisely due to interactions on the molecular scale. Two materials, containing crown ether macrocycles (CyHz1 and CyHz0) served as COF building blocks to give two different pseudorotaxane-based COFs, namely RCOF-1 and RCOF-0 [126]. Methyl viologen hexafluorophosphate (MVPF6) interacts with the crown ether rings of RCOFs to form pseudorotaxane complexes. The insertion of viologen molecules induced charge transfer, which greatly decreased the molecular dipole between COF layers. At the same time, steric hindrance and electrostatic repulsion weakened π-π stacking between layers, promoting COF exfoliation. The exfoliated RCOF-0 exhibited thickness of monolayer unit cell (2 nm thick), due to their asymmetric tortuous surface, which eliminated the molecular dipole effect for minimizing the interlayer interaction. In RCOF-1, there were still anti-parallel stacked molecular dipoles between each layer of the unit cells, giving an exfoliated thickness corresponding to a bilayer unit cell (4 nm thick) (Fig. 5b). This crown ether macrocycle could provide extra functional groups, but it would occupy the space of pore channel in COFs, and hence impeding the accessibility of the reactants.

(5) Selective decomposition of dual-pore COFs. Due to differences in chemical stability of bonds and pore structure of heteropore COFs, organic nanotubes can be manufactured by selective hydrolysis one of the linkages while keeping the other untouched [127]. The shape and size of nanotubes resulted are thus precisely designed, predicted, and controlled. A dual-pore COF containing hydrazone and boroxine linkages was constructed via orthogonal reactions [128]. Individual organic nanotubes with hydrazone-linked macrocycles could be generated through hydrolyzing boroxine linkages. It may induce fully/partially disordered arrays and even affect the conductivity of COF, making therm difficult understand structure-performancs relationships. Nanotube array is expected to solve the dilemma.

Mechanical exfoliation. Mechanically grinding of COFs using mortars or ball mills can disrupt the interlayer interaction forces to produce CONs. This method is simple, requires lesser preparation time, and can be adapted for mass production. However, the thicknesses and yields of the prepared nanosheets are not as ideal. Interestingly, Banerjee's groups developed a simple energy-saving and environmentally friendly mechanochemical grinding method to exfoliate eight different kinds of COFs [129,130]. This method can be carried out in a relatively mild condition without special requirements (e.g., inert atmospheres, dry solvents, and expensive supports). Compared to manual mortars and pestles, ball milling endows mechanical exfoliation with automation, thus controllability. Grinding the anthraquinone-based COFs via ball milling at 50 Hz, the DAAQ-ECOF was exfoliated with a thickness of 3-5 nm, which was tunable by controlling the vibration frequency and time [131]. Relatively, the crystallinity of COF NSs obtained by mechanical exfoliations is relatively poor.

In the process of preparing various 2D COF NSs, top-down strategy including solvent-assisted exfoliation and mechanical exfoliation often resulted in uncontrollable thicknesses, sizes and mechanical damages. Stacking layers undergo interlayer shifting [121,132], changing COFs inherent properties and rendering the structural analysis more difficult. Alternative options should be considered to maintain a balance between exfoliating and re-stacking.

Large-scale and/or rapid synthesis

Large-scale and rapid fabrication of high-quality COFs is a prerequisite for practical applications. The COF preparation usually utilizes low monomer concentrations at laboratory scale, which needs to be translated to a large-scale fabrication. Large-scale and rapid synthesis can effectively reduce cost and time, which is essential for the industrial production of COFs. Several strategies for large-scale and rapid preparations of COFs have been investigated, which encouraged the exploration of COFs toward industrial applications. Although some impressive results have been obtained, large-scale synthesis is undeniably still in its infancy.

Catalytic rapid synthesis. Developing novel catalysts to promote COFs synthesis effectively lessen cost and duration. Although *p*-toluenesulfonic acid (PTSA) catalysts possess many advantages for catalyzing solid-state reactions in COF synthesis [133,134], large amount of PTSAs is required for scaled production, which results in high costs and tedious recycling steps. Imine-linked COFs can be rapidly synthesized arising from the catalytic effects of metal triflates, notably catalysts ($Sc(OTf)_3$) containing costly rare-earth element, scandium [135]. Transition metal nitrate catalysts ($Fe(NO_3)_3{\cdot}9H_2O$) provide a cheaper alternatives to rapidly synthesize TAPB-Dma COFs within 10 minutes at ambient conditions, and the reaction process was not sensitive to oxygen or water [136]. Selected Fe-NO catalyst is general to synthesize a series of COFs with different stabilities containing varying linkers lengths and functional groups.

Electron beam rapid synthesis. Conditions required to synthesize COFs are harsh and tedious (high temperature, high pressure and long reaction time) making them difficult to be adapted for industrial production [120]. High-energy ionizing radiation (such as electron beams and γ rays) can be used to synthesize and modify a large number of functional materials, including inorganic nanoparticles and amorphous polymers [137,138]. Compared with traditional solvothermal method, energy consumption of ultra-rapid synthesis by electron beam irradiation may be reduced by two orders of magnitude and the entire process occurs within a few minutes. A high-energy electron beam of 1.5 MeV induced EB-COF-1 crystalline with the yield of 92% within a short time frame of 160 s under ambient conditions (Fig. 6a) [139]. Strong and targeted energies on the reactants overcame the activation barriers and ionized the entire reaction system. The reaction between benzaldehyde and radiation-produced imino radical ($C_6H_5{-}NH{\cdot}$) occurs rapidly with significantly reduced

energy barrier (E_a) for the rate-limiting step of C−N bond formation. As a result, the production of COFs was close to quantitative yield. In addition, a series of COFs, such as COF-SDU1 [140], TPT-BD COF [141], COF-JLU7 [142] and COF-DhaTab [143], were successfully synthesized in nearly quantitative yields under ambient conditions using the same method. Therefore, this method endows great potential for industrial mass production of COF crystals.

Dipole-induced antiparallel stacking. Self-correction processes can minimize errors in the course of forming crystalline COFs. Growth errors stem from the hyperbranching caused by molecular rotations of linkages within building blocks, and random stacking of substrates with different energy content. Anti-parallel stackings with intra- and inter-layer hydrogen bonds restrict intramolecular bonds rotation, thus promoting rapid COF growth. Under this guidance, gram-scale (up to 1.4 grams) acylhydrazone COFs (Tf-DHzOAll and Tf-DHzOPrY COFs) were produced within 30 minutes, which supported hydrazide ligands with different side chain functionalities [144]. The forming intralayer hydrogen bonds (N-H···O) restrict rotations of molecular bonds to form a rigid structure and allow covalent framework to extend along the 2D plane. In-plane rigidity enabled bonding dipole moment in the plane, promoting anti-parallel stacking corresponding to the lowest total energy. Furthermore, interlayer electrostatic interaction via charge repulsion was avoided.

Hierarchical-coassembly-enabled 3D-printing. The supramolecular Pluronic F127 and functional small molecules can be co-assembled for the synthesis of 3D-printable hydrogels, which show unique characteristics (e.g., shear thinning and fast self-healing). After post-printing collaborative assembly, covalent cross-linking, and the removal of printing template, additive manufacturing, including inorganic, organic, and inorganic/organic hybridized small molecules, was carried out [145]. A 3D-printing hydrogel was formed by limited polymerization of imine polymers and subsequently, their co-assembling with 3D printing template Pluronic F127 [146]. Additive-free 3D-TpPa-1, β-ketoamine-linked 3D-TpBD-Me_2 and imine-linked 3D-TPE-COF were obtained with complex macrostructure, crystallinity and pore sizes ranging from a few nanometers to submicrometer. This method can also be used to combine multi-component COF into one substrate. Cross-linking at COF/COF interface allows two distinct COF materials to be covalently connected to each

other, since the reversible Schiff base exchange reaction typically occurs at the interface regions (Fig. 6b). 3D-printing COFs not only had complex macrostructures with high mechanical strengths, crystallinities and surface areas, but also connects multi-component 3D-COFs together at the molecular level. Therefore, 3D printing technology is a versatile tool to extent COF materials for wider application purposes. Processes for 3D-printed COF materials still rely heavily on manual operation. The use of artificial intelligence for large-scale fabrication of COFs is a promising direction that renders further exploration.

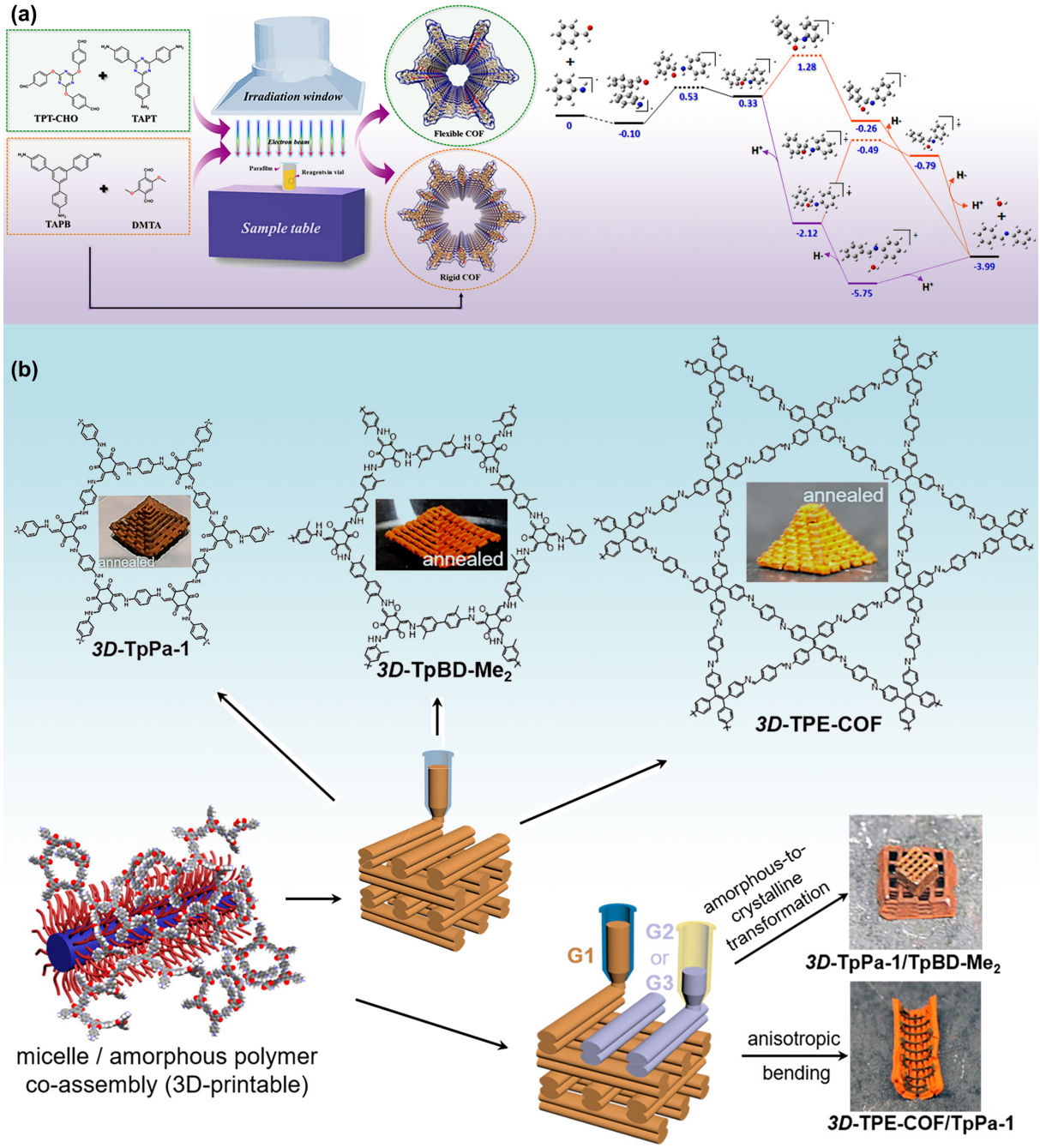

FIGURE 6. (a) Left: COFs synthesized by electron beam irradiation; Right: energy profiles of the reaction pathway under irradiations. (b) Designing and synthesizing imine- and β-ketoenamine-linked COFs/COF monoliths by the supramolecular templated co-assembly method. Reproduced with permission [139] and [146]. Copyright 2019, 2020, American Chemical Society.

To date, the methods for synthesizing COFs that have been proposed are far from meeting the requirements of practical applications in views of economic cost, time and yields. Additionally, the large-scale synthesis of single-crystal COFs is still extremely challenging. Although a ventilation-vial protocol was proposed to achieve gram-scale yield (2.0 g) of single-crystal COF-300-V [147], the forming mechanisms and factor of amplification for high yields is recommended to be explored in depth.

Structure−performance correlation to guide the applications of COFs

Having the continuous breakthroughs in synthesis processes, such as stability, yield, and scalability, COFs with different structures and properties have been manufactured and used in numerous application fields [148]. However, in-depth understanding of the correlation between structure and performance in various fields is still lacking, which severely limits the practical application of COFs. Therefore, a systematical discussion on the structure-performance correlation is necessary to help in the developing field of COFs.

Correlation between COFs and catalytic performance

The diversity of skeletons and pores in COFs allow for constructing multitudinous heterogeneous catalysts using different chemistries [149]. Expanded molecular framework can be tailored for diverse functions central to accelerating the reactions of bond-cleaving and forming [150]. Thus, structural advantages of COFs make them promising candidates as stable catalyst with excellent catalytic activity and selectivity [22,151].

COFs can be utilized for a wide variety of catalysis including chemical catalysis, biocatalysis, electrocatalysis, photocatalysis, depending on their properties, such as crystallinity, morphology, light capture ability, charge separation and migration, proximity of

sacrificial electron donor (SED) and co-catalyst [152–157]. Interestingly, both twisting the angle (i.e., torsional angles of the central aryl rings with the peripheral phenyl rings in linkers) and donor-acceptor conjugation can directly affect the properties and activity of the resultant COF catalysts [158,159]. Dopants modify charge properties of COFs by forming supramolecular charge-transfer complex, which flatten the energy band and localize the electronic state [160]. Porosity improves reactant accessibility and highly ordered domains ensure suitable capacity for charge percolation and charge carriers trapping at defective sites [150].

Predesigned functionality and composition. Tailor-made framework wall with predesigned functionality and composition can improve catalytic selectivity [161,162]. Incorporation of electron-deficient units into layered 2D lattice periphery has a profound impact on the border orbital, band structure and heterojunction interface, effectively regulating the electronic and photoelectric properties of COFs [163]. Many functional groups, including aromatic units, acetyl, hydroxyl, alkyl chains, chromophoric moieties and ester, have been introduced to framework walls [164]. Halogen substitution in the building blocks of COFs tuned the photoelectrical conversion and charge carrier mobility. After the introduction of halogen atoms (F and Cl) into COFs, photocatalytic performance of HER for resulting Py-ClTP-BT-COF (177.50 μmol h^{-1}) and Py-FTP-BT-COF (57.50 μmol h^{-1}) was 8.2 and 2.7 times higher than that of non-halogenated Py-HTP-BT-COF (21.56 μmol h^{-1}), respectively [165]. And Py-ClTP-BT-COF exhibited high apparent quantum efficiency (AQE) of 8.45% at 420 nm. Under the conditions of visible light excitation, the introduction of halogen atoms promoted the efficient separation of photogenerated electrons and holes, resulting in the generation of more photogenerated carriers to participate in water splitting reaction. Simultaneously, the α-carbon atom linked to the halogen atom served as an active site for proton reduction to lower the energy barriers for forming H* species in the reduction reaction.

The participation of multiple groups may have a better effect than a single group. Three isostructural COFs were manufactured via modifying by different functional groups (OMe-TPBP-COF (containing methoxy), OMe-OH-TPBP-COF (containing methoxy and hydroxy) and OH-TPBP-COF (containing hydroxyl)) to form docking sites in their porous channels. The yields for CO_2 cycloaddition with various epoxides were 91%, 89%, and 48%,

respectively [166]. The methoxy groups with greater steric hindrance limited the rotation of two benzene rings along the C-C bond in the biphenyl moieties, resulting in better thermal stability for OMe-OH-TPBP-COF. The hydrogen atom of the hydroxyl groups and the oxygen atom of the epoxides form a hydrogen bond, which facilitated the polarization of the C-O bond for epoxides. OMe-OH-TPBP-COF possessed the best catalytic performance due to enhanced stability, better crystallinity and greater surface area.

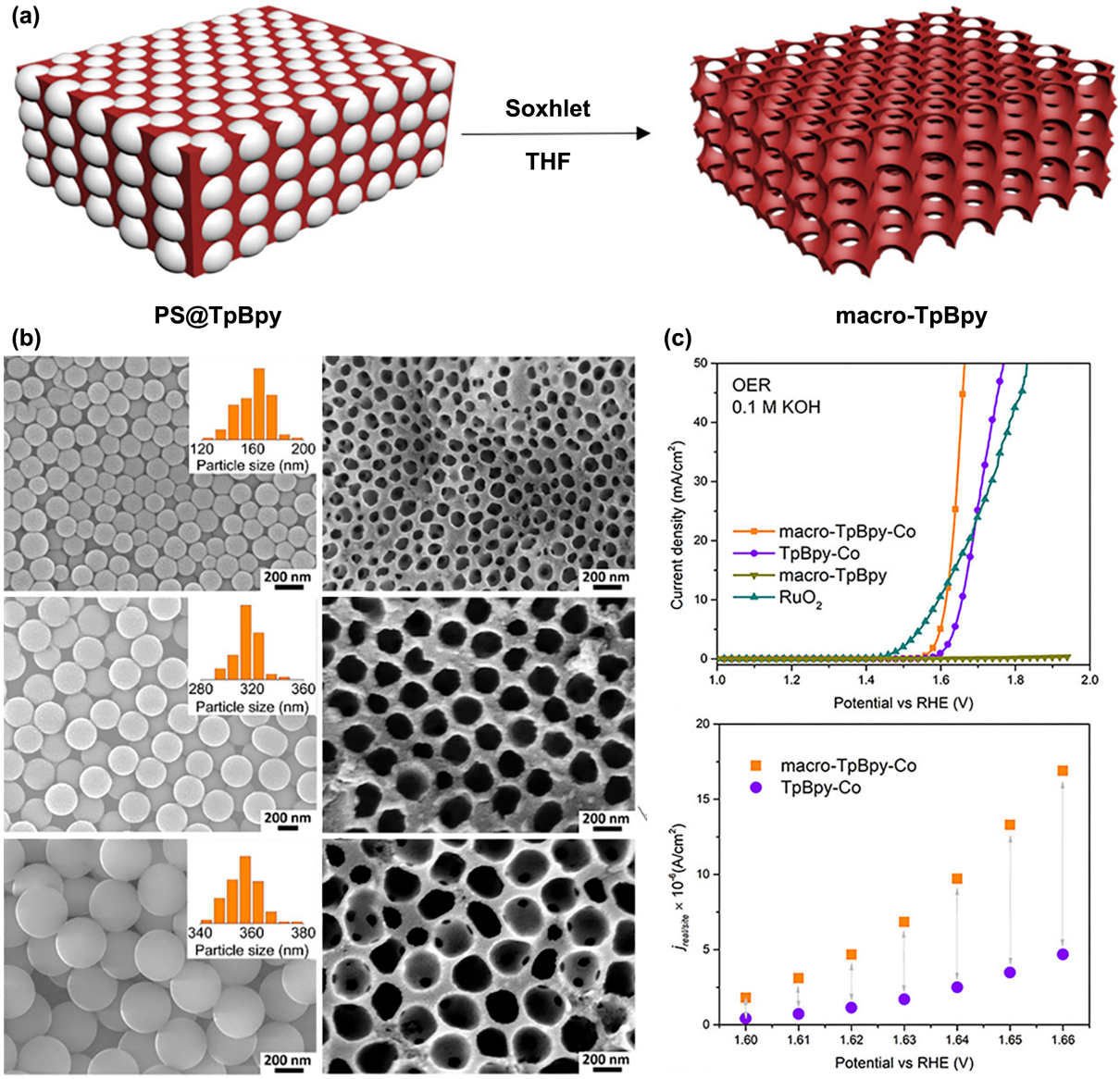

FIGURE 7. (a) Synthesis of macro−microporous COF. (b) SEM images of PSs and macro-TpBpy. (c) OER performance of macro-COF-Co. Reproduced with permission [170]. Copyright 2019, American Chemical Society.

Pore enrichment and sizes. The pore structure and the interior functional groups of porous materials have a characteristic effect on the adsorption of small gas molecules. Significantly increasing local gas molecule concentrations in the pores can promote their catalytic reaction inside porous materials [167]. Pore size as well as pore distribution in COFs is also important for the selective diffusion of reactants or products through the aperture o give catalytic selectivity. 3D microporous BF-COF-2 with the rectangular apertures of 7.7×10.5 $Å^2$, catalyzed benzaldehyde (6.1×8.7 $Å^2$) into 2-benzylidenemalononitrile with high conversion rates of 98%, while the conversion rates of 4-phenylbenzaldehyde (6.1×13.3 $Å^2$) was only 2-4% [168]. This was attributed to the size mismatch between molecules and pore aperture, making it hard for the substrates to enter the channels and for the products to leave the pores.

COFs mainly possess microporosity, which might cause mass transfer limitation and low utilization of active sites. Hierarchical pores in COFs provide a viable solution for rapid mass transfer. The larger pores facilitate guest molecules transport and the inner small micropores provide enough surface area and active sites for reaction to occur [169]. Zhao et al. prepared various crystalline β-ketoamine-based COFs with macropores and microporosity, whose macroporous sizes range from 160 nm to 360 nm (Fig. 7a, b) [170]. The prepared highly crystalline macro-TpBpy achieved rapid mass transports as well as openly accessible reaction sites due to the different pore types. Remarkably, the electrocatalytic oxygen evolution reaction (OER) performance of macro-TpBpy was much higher than that of pure microporous TpBpy. This could arise from the improved guest molecules diffusion due to the homogeneous and interconnected hierarchical pore channels, making active Co^{2+}-bipyridine sites easy to access (Fig. 7c).

Crystallinity. Crystallinity of COFs has significant impact on its catalytic activity. Better crystallinity results in more ordered covalently bridged framework, which is beneficial to the expansion and/or stacking of π system, as well as the transverse and/or vertical transport of charge carriers. Within larger ordered domains, excitons possess much stronger degrees of diffusion freedom and lower surface traps per excitation density [171]. It has been proven that N2-COF sample with lower crystallinity generally resulted in poor porosity and a lower HER rate [149]. The lower crystallinity and porosity likely lead to smaller π-systems extensions or/and stacking defects, hindering the in-plane or/and vertical transport of charge carriers

within the COF photosensitizer, and also reduced accessibility of co-catalyst, limiting interfacial charges transfer from N2-COF to cobaloxime. Remarkably, good crystallinity is also capable of improving the light absorption and promoting the dissociation of photoinduced excitons. Crystalline Py-Td COFs exhibited enhanced photocatalytic activity for alpha-terpinene to ascaridole than that of amorphous counterparts, Py-Td-POP [172]. This result was attributed to the improved light absorbability and photogenerated electron and hole pair separation of crystalline Py-Td COFs.

Coordination environment. Well-tunable coordination environments (basic/acidic sites) in the π-conjugated skeleton are usually impetus to the catalytically active centers [159,173]. By increasing the density of active centers available, as well as the extent of framework conjugation, catalytic performance can be greatly enhanced. According to the principle of coordination chemistry, strong interactions (σ dative bonds) between ligands and metal ions can endow COFs with specific catalytic activity, due to metal-ligand charge transfer [174]. COFs containing phthalocyanines and pyrazine can anchor transition-metal (TM) atoms firmly without migration and aggregation [175,176]. To date, many other similar organic sites (e.g., bicatechol and bipyridine components, porphyrin units, phthalocyanines, pyrazine, and interlamellar nitrogen) were thoroughly investigated [16,177–180]. Metal-ligand charge transfer is also crucial for photocatalytic reactions [181–183]. It was found that porphyrin-based COFs coordinated with Zn^{2+} exhibited superior photocatalytic terpinene conversion of 99% [184], compared to DhaTph-2H (70%) and DhaTph-Ni (7%). The higher selectivity was attributed to the more efficient $^1O_2$ generation. Incorporation of Zn^{2+} into COFs was beneficial to converse singlet to triplet excitons, resulting in the activation of O_2 to $^1O_2$, while introducing Ni^{2+} promotes the dissociation of excitons to hot carriers under photoexcitation, thereby activating O_2 to $O_2^{\bullet-}$ instead. Therefore, different activities and selectivity were observed for the photocatalytic oxidation of terpinene by DhaTph-M species.

However, metal coordination interaction may lower the crystallinity and porosity of COFs [16,185]. Notably, our previous research showed that stability and crystallinity of COFs (M/COF-DB), formed via supramolecular intra- and inter-molecular hydrogen bonds, along with electrostatic interactions in the antiparallel stacking mode, can be improved after metal coordination compared with the parent COF−DB [186]. Different transition metal ions (M =

Mn, Co, Ni, Cu, Zn, Pd, and Cd) coordinated with appropriate nitrogen sites in COF-DB under mild conditions result in M/COF-DB with extended π-conjugations, enhanced crystallinities, increased stabilities and extra functionalization. Additionally, spin states of transition metal sites in COFs largely affect their photocatalytic performance [187,188]. Spin states influence density-of-state coupling of atomic orbitals between the metal in COFs and the target molecules, thereby affecting the energy barrier of intermediate step.

Intercalation of bimetallic active sites may break the restriction of scaling relations (such as similar bond formation and adsorption behavior) and significantly improve the electrocatalytic activities. Gong et al. proposed a class of bimetallic-atom electrocatalysts (BACs) with bimetallic 3d transition metal active sites within COFs channels, which were more efficient than noble metals and single-atom electrocatalysts (SACs) for CO_2 reduction reaction (CO_2RR) [189]. It was found that the Fe/Cu- and Ni/Zn-BAC-COFs act as excellent BAC-COF electrocatalysts for CO_2RR, with their low overpotential (~0.25 V) suppressing HER side reactions (η^{H2} = 0.51 V). Synergistic effects of bimetallic active centers allow the intermediates (*CO_2, *COOH and *CO) to reach an almost perfect adsorption/desorption state, thus enhancing the catalytic CO_2RR performance. However, further investigation regarding the spatial locations (external or internal attachment) and numbers of metal active sites in COFs is required to further exploration to get a clearer picture of the full mechanism at work.

Chemistry of ligands. Organic ligands in COFs differ in their catalytic activity. Generally, geometries of building blocks dominate the development of rudimentary frameworks. Different ligands can easily tune the various properties of COFs, including crystallinity, morphology, porosity, hydrophilicity/hydrophobicity, π-conjugated stacking, band gap, light absorption ability, optoelectronic properties, energy levels, etc [190]. The incorporation of electron-deficient unit may facilitate energy absorption and electron transfer [191]. Extended π-conjugated skeleton of COFs resulted by the favorable ligands can exhibit the enhanced light-harvesting ability [192]. Using different types and functional domains present on COF ligands, one can anchor active sites suitable for catalytic performance to improve catalytic efficiency. Pentacyclic thiophene-sulfur building blocks in MFTS-COFs were utilized as active center for oxygen reduction reactions (ORR) [193]. Compared to thiophene-free COFs

(PDA-TAPB-COF), MFTS-COFs exhibited a higher catalytic efficiency due to their higher electron transfer numbers, narrower band gaps and lower overpotentials. Therefore, MFTS-COFs with higher thiophene sulfur content shows better ORR performance.

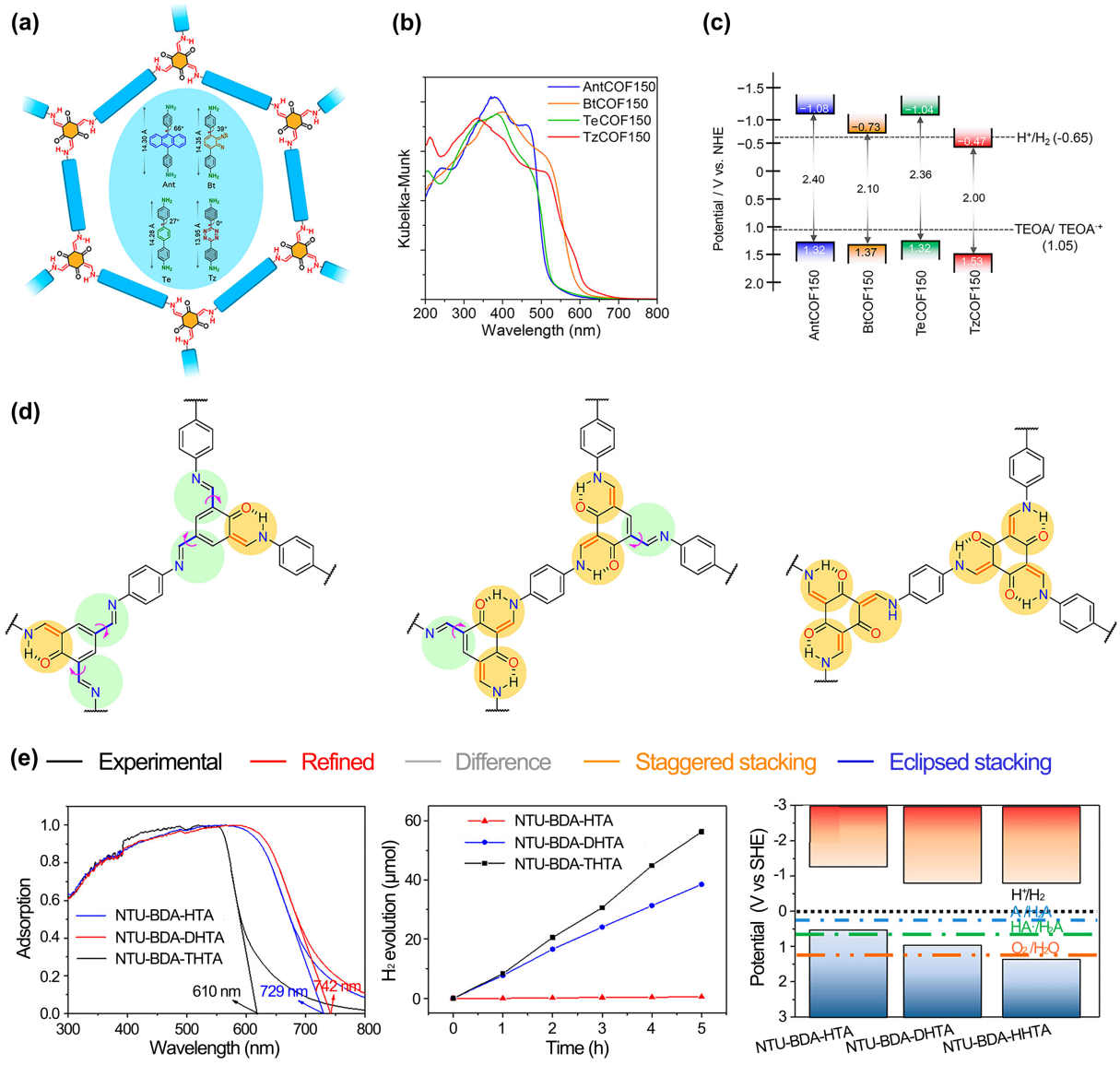

FIGURE 8. (a) Chemical structures of 2D COFs. (b) UV−vis diffuse reflectance spectra of COFs. (c) Band positions and band gaps of COFs vs NHE at pH 11. (d) Various ratios of *β*-ketoenamine (orange) to imine (blue) moieties in unit cell of COFs. (e) UV–vis-DRS spectra, photocatalytic H_2 evolution performance and energy band potentials of these three COFs (NTU−BDA−HTA, NTU−BDA−DHTA and NTU−BDA−THTA). Reproduced with permission [158] and [210]. Copyright 2020, American Chemical Society.

Similarly, Ghosh et al. designed a series of β-ketoenamine-linked isoreticular 2D COF catalysts (such as TeCOF, AntCOF, BtCOF and TzCOF) by replacing 4,4"-diamino-substituted *p*-terphenyl (Te) center ring with electron-rich anthracene (Ant), electron-deficient benzothiadiazole (Bt), and tetrazine (Tz) π-conjugated skeleton [158]. The torsional angles between the central aryl rings (Te, Ant, Bt and Tz) and the peripheral benzene rings were 27°, 66°, 39° and 0° (Fig. 8a), respectively. As a result, these COFs had different physical (surface area, crystallinity, stacking mode, etc.) and photoelectric properties (light harvesting ability, band gap, charge separation, etc.) (Fig. 8b, c). The average HER rates of TzCOF, AntCOF, TeCOF, and BtCOF were nil, 55 ± 5, 50 ± 4, and 750 ± 25 μmol h^{-1} g^{-1}, respectively. The cumulative effect of larger surface areas, favorable stacking, as well as increased light absorption capacities and charge carrier mobilities, arise from the introduction of benzothiadiazole-containing ligand, resulting in improved photocatalytic activity of BtCOF.

Interestingly, changing the geometric symmetries of units in the conjugated frameworks also affects semiconducting behaviors, as seen from vinylene-linked g-$C_{54}N_6$-COF and g-$C_{52}N_6$-COF. The average O_2 and H_2 evolution rates of high-symmetric g-$C_{54}N_6$-COF were 51.0 and 2518.9 μmol h^{-1} g^{-1}, respectively, which were much faster than less-symmetric g-$C_{52}N_6$-COF (12.5 and 1171.9 μmol h^{-1} g^{-1}, respectively) [194]. This was attributed to the octupolar conjugated structure arising from symmetry structure, and hence resulting in outstanding photo-induced charge generation, transfer and separation.

Layered structure and stacking modes. Different stacking modes can change the reaction energetics of intermediates and the transfer of charge carriers, because of the varying interlayer van der Waals and π–π stacking interactions, to modulate catalytic activity [195]. The steric exclusion between adjacent hydrogen atoms could be overcome by layered π-π stacking, and high charge carrier mobility could arise from the π-electron conjugation in-plane, as well as possible π-orbital overlap, leading to the transport of axial charge along the stacking direction. Therefore, COFs are promising supramolecular architectures to achieve effective light harvesting and charge transport [196]. Different layered stackings (eclipsed, inclined, and serrated) influence the pore geometry in the functional region of COFs, resulting in different electronic properties of materials [197]. Interlayer spacing is one of the key

factors that contribute to carrier transport and conductivity. The charge carrier mobility of TTF-Ph-COF with an interlayer distance of 3.71 Å, was 0.2 cm^2 V^{-1} s^{-1} is higher than that of TTF-Py-COF with a larger interlayer distance of 3.83 Å (0.08 cm^2 V^{-1} s^{-1}) [198]. On the contrary, relative to pyridine-free POR-COFs (4.4 Å), the presence of pyridine cocrystallization expanded the interlayer distance of Py-POR-COFs (5.6 Å) and enable oxygen species to access the interlayer space [199]. Such architectures enable the energetics of ORR intermediates and affect scaling relations among different kinds of reaction intermediates. The proper stacking modes and interlayer spacing still need to be further investigated.

Dimensionality. Dimensional diversity also affected resultant COFs properties, such that their catalytic activities. Dimensionality indirectly influences other structural properties, such as surface area, porosity, crystallinity, which change the resultant ion conductivity, carrier mobility, mass transfer and optical properties. COFs typically exist in 2D and 3D, with varying structural architecture. The covalent bonds of 2D COFs only exist in plane with the one-dimensional (1D) pore channels [200], with interlayer stackings formed via noncovalent interactions, such as van der Waals coupling, hydrogen bonding and π-π stacking. On the other hand, 3D COFs are made entirely out of covalent bonds [173]. Complicated pore structures endow 3D COFs with greater surface area, lower density, and more accessibly open active sites compared to 2D COFs [59].

For 1D COFs, it is often difficult to control their morphology, as the extension and alignment of atomic layers may be impaired from the spatial constrained growth in a single direction [201]. Zero-dimensional (0D) COFs are difficult to synthesize and mostly amorphous on microscale [202]. Thus, 1D COFs and 0D quantum dots (QDs) COFs are rarely studied. 1D linear and fibrous COFs were recently synthesized and endowed with anisotropic properties due to specific interactions between triazine and pyrene [100,203,204]. The formation of long-range protons conduction paths could enhance proton conductivity [205]. 0D COF QDs possess low toxicity, tunable structures, long fluorescence lifetimes, and high chemical stability [206]. However, limited studies on the catalytic capacity of low-dimensional COFs are available to generalize findings.

Preliminary studies found different catalytic performance by comparing 2D and 3D COFs. Meng and co-workers compared between 2D and 3D palladium porphyrin-based COFs, namely 2D- and 3D-PdPor-COF [207]. Both COFs exhibited similar crystallinity, thermal stability, structure and morphology. Under visible light induced sulfide oxidation, 3D-PdPor-COF gives an enhanced yield of 98%, much higher than that of 2D-PdPor-COF (48%). The triplet excited state was sufficiently quenched in 2D-PdPor-COF due to the eclipsed AA stacking mode of palladium porphyrin units, while 3D-PdPor-COF with a five-fold interpenetrated *pts* topology can effectively generate peroxide radical anions. This resulted in the discrepancy in catalytic activities for the 2 species. However, catalytic yield of 3D-PdPor-COF lowered drastically (48% for 4-tert-butylphenyl methyl sulfide) for larger size of the substrate, due to size-selectivity arising from its small pore size (0.58 nm). These differing point-of-views and phenomena provide possibility for the future exploration of catalytic performance with COFs of different dimension. Also, it is a promising direction to investigate photocatalytic performance of 0D and 1D COFs to strengthen the correlation between dimensionality diversity and catalytic performance.

Linkage. Dynamic and robust linkages in COFs enables stability, crystallinity, diversity etc. within the framework structure [173], and also fine-tuned the pore environment, morphology and functions in the extended skeletons. Compared with imine- or arylhydrazone-linked COFs with relatively lower stability and poor π-delocalization, olefin-linked COFs possess excellent stability and photo-electrochemical performance [208]. Comparing three types of isostructural COFs with different linkages (i.e., COF–alkene, COF–imide and COF–imine), the photocatalytic performance is as followed: COF–alkene (stable 2330 μmol h^{-1} g^{-1}) >> COF–imide (34 μmol h^{-1} g^{-1}) > COF–imine (12 μmol h^{-1} g^{-1}) [209]. The COF–alkene, with stronger intramolecular charge transfer in the skeleton and larger photogenerated electron population (electron polarons) had an AQE of 6.7% at 420 nm. With electron-withdrawing cyano-substituent closely attached to the alkene linkage, and electron-donating triphenyl in the framework, the donor-acceptor molecular heterojunction to allow effective electron transfer via a powerful push–pull interaction.

Our research group has investigated the relationships between different ratios of β-ketoenamine to imine linkage, using NTU−BDA−HTA (2:4), NTU−BDA−DHTA (4:2) and

NTU−BDA−THTA (6:0) (Fig. 8d) [210]. Structural periodicity, band gap and visible light harvesting properties could change due to the different ratio of linkages used. Our group has proved that the structural order and light absorbing capability of all three COFs have little effect on the photocatalytic performance, with PHE performance of NTU-BDA-THTA, NTU-BDA-DHTA and NTU-BDA-HTA at 1.47 μmol h^{-1} m^{-2}, 0.60 μmol h^{-1} m^{-2} and 0.0087 μmol h^{-1} m^{-2} respectively. The imine moiety in NTU-BDA-DHTA and NTU-BDA-HTA has a suppression effect on the excited state of the mixed bond, resulting in the PHE performance trend. As the β-ketoenamine bond containing more 2p O atoms increases, the more favorable positive potential of the highest occupied molecular orbital (HOMO) energy enhanced the oxidizing power of the photogenerated holes, allowing easier interaction with the hydrogen bond of L-ascorbic acid in NTU−BDA−THTA (Fig. 8e). In order to achieve overall water splitting, catalytically active molecular segments for OER and HER can be introduced into COFs skeleton via topological means [211].

Morphological control is considered to be a powerful tool to tune the catalytic properties of heterogeneous COFs, being responsible for band gap structure, charge separation along the extended π-conjugated skeleton [212], as well as light absorbance [213]. Moreover, the catalytic efficiency and product selectivity of COFs catalyst can be modified by building the recognizable active sites and surface engineering. In addition to the single structural changes in COFs, the combination of defects, 3D COF, morphology and reactive variation still require further investigations for a more complete picture of the complex synergistic interactions. Constructing the organic/inorganic heterojunction catalysts may contribute to improve the catalytic performance of COFs. How to effectively convert the laboratory results of COFs photocatalyst into the practical devices is still a great challenge.

Correlation between COFs and energy storage

Batteries are made up of anode, cathode, electrolyte as well as separator, to convert chemical energy into electric energy. Utilizing porous membranes as separators can prevent short circuits, by allowing ions are able to pass through while restricting electrons movement. Supercapacitor can store energy by forming a double-layer interface between the electrode and the electrolyte. COFs have been applied for energy storage application due to their

relatively high capacity and superior electronic properties, which could be utilized as either electrode materials for supercapacitor, battery or fuel cells [214–216]. However, COFs have some drawbacks, including structural defects, as well as poor ion mobility and energy level matching, which are not conducive to the construction of electrode materials [217]. Nevertheless, many stable and conjugated COFs with characteristic wire skeleton along with open nanochannels have been developed [218–220], and two-dimensional sheets were spanned with π conjugation. Those COFs show many favorable properties, such as extended π-delocalization, holes mobility, accommodation of guest molecules and chemical stability. Fully conjugated COFs also has superior conductivity and uniform porosity for the transport of guest molecules [221,222].

For lithium-sulfur batteries, an inherent common problem known as the shuttle effect limits their efficiency in practical applications. During the charging and discharging process, polysulfide (PS) intermediates produced by the positive electrode dissolves into the electrolyte, penetrates the diaphragm and diffuses to the negative electrode. It further reacts with lithium directly at the negative electrode, which ultimately results in irreversible loss of effective substances, decay of battery life, and low Coulomb efficiency [223]. Tuning active centers that effectively block polysulfides using COFs can enhance the performance of battery. This can be achieved by introducing reactive functional groups into COFs to chemically bond with sulfur [224,225], or combining skeletons with multisulfur chain to enhance the interaction between skeletons and polysulfides [226].

Linkages. For cathode materials, polar linkages of COFs could have a powerful anchoring capability, which could trap polysulfides (Li_2S_x series, x = 4, 6, and 8) through adsorption interaction between polar linkages and Li_2S_x, thereby impeding the shuttle effect of polysulfides and enhancing the performance of batteries [223]. Both COF-SA with secondary amine linkages and COF-Hy with hydrazone linkages possess powerful anchoring capacity on Li_2S_x series [227]. The two O atoms in the secondary amine linkage had synergistic effect, allowing them to effectively gain electrons from S atoms in Li_2S_4. The interaction of COF-Hy with Li_2S_4 was primarily through both Li-N and Li-O bonds. Simultaneously, the “clamp” structure (N1−N2−C−O1) of COF-Hy containing hydrazone linkages could greatly enhance electron-grasping ability. Compared to conventional lithium-ion batteries (LIBs), which use of

liquid electrolytes, all-solid-state LIBs possess superior electrical performance in terms of safety and long-term stability [228]. *β*-Ketoenamine-linked COF-TRO as the cathode material for an all-solid-state LIB achieved a near theoretical specific capacity of 268 mAh g^{-1} [229]. The energy density of COF-TRO cathode materials was 415.4 Wh kg^{-1}, much higher than other COF materials, such as phenazine-based DAPH-TFP COF [230] (221.26 Wh kg^{-1}) and anthracene-based IISERP-CON2 [231] (364 Wh kg^{-1}). Furthermore, the battery displayed outstanding stability, with the coulombic efficiency remained at 99.9 % after 100 cycles. In the lithiation/delithiation process, primary electron acceptors within COF-TRO were truxenone moieties. The Li^+ could be closely hosted by truxenone within narrow voltage through electrostatic interactions. Li^+ storage was greatly improved due to the ordered crystalline COF structures with high-density redox-active carbonyl groups.

Number of stacking layers. COFs with differing number of layers feature distinct channels, conductivity and exposed active sites, which affect the ions/electrons transfer and storage. DA-COF has excellent carrier mobility, large anisotropic photoconductivity in the vertical direction [232]. Carrier mobility of DA-COF is dependent on the number of layers and stacking order. The total energy of AB-stacking was higher than that of the AA-stacking and thus, ambipolar transport of electrons and holes can be easily achieved due to strong vertical conductivities along the stacking axis. The band gap of AA-stacked DA-COF decreased with increasing number of stacked layers (1.73, 1.23 and 0.25 eV in monolayer, bi-layer and bulk DA-COF, respectively). In contrast, the charge transfer along the vertical direction of DA-COF increased with increasing number of stacking layers (0.82 |e|, 1.22 |e|, and 1.30 |e| for monolayer, bilayer, and bulk DA-COF, respectively). In addition, intralayer charge transfer enhances with increasing interlayer interactions due to adjacent-layer electron hopping, which remarkably changed the electronic band structure.

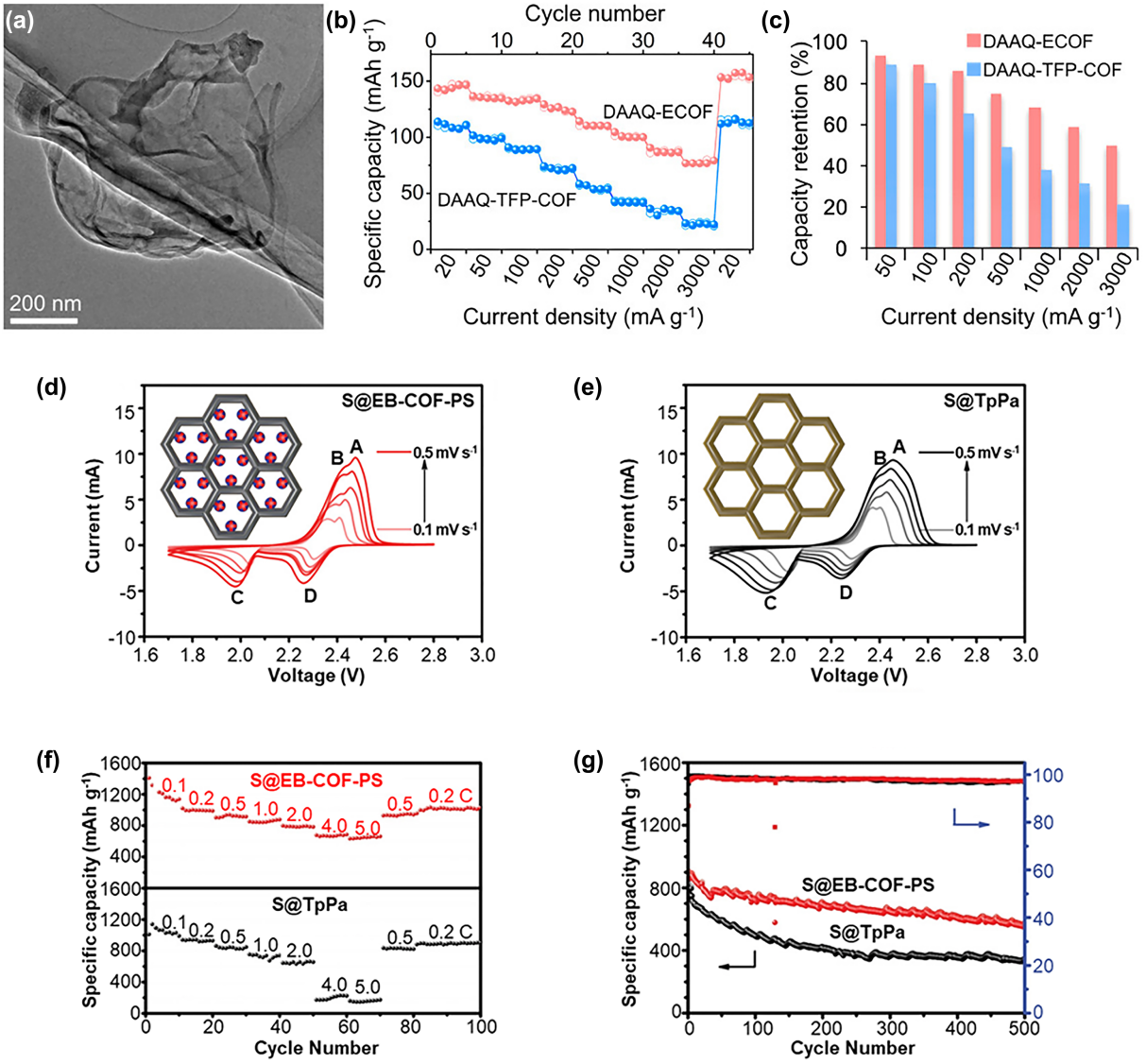

FIGURE 9. (a) TEM of DAAQ-ECOF. (b) Rate cyclability and (c) capacity retention relative to capacity at 20 mA g^{-1} for DAAQ-ECOF and DAAQ-TFP-COF. Reproduced with permission [131]. Copyright 2017, American Chemical Society. Cyclic voltammetry profiles at different scanning rates of cells with (d) S@EB-COF-PS and (e) S@TpPa cathodes. (f) Rate performances at diverse current densities and (g) galvanostatic charge–discharge cycles at 0.5 C for S@EB-COF-PS and S@TpPa. Reproduced with permission [235]. Copyright 2020, John Wiley & Sons, Inc.

It is difficult for Li/K ions to penetrate through the active sites in the tightly stacked bulk COFs, even at high-current density. Utilizing few-layer thick COF nanosheets can achieve superior potassium storage performance [233], because of the enhanced π–π stacking and

numerous exposed active sites to reduce ion/electron diffusion distance and to improve K^+ insertion/extraction kinetics. Similarly, the thickness of DAAQ-ECOF cathode decide the performance of LIBs. Compared to bulk DAAQ-TFP-COF (110 mAh g^{-1} at 20 mA g^{-1}), DAAQ-ECOF nanosheets showed higher reversible capacity (145 mA h g^{-1} at 20 mA g^{-1}), with good rechargeability (capacity retention of 98% after 1800 cycles) and higher charge−discharge capabilities (Fig. 9a-c) [131]. The shortened diffusion pathway and exposed active sites of few-layer thick DAAQ-ECOF bearing ultrathin 2D nanosheets are effective for Li^+ diffusion and storage.

Ionization. To reduce rapid decay of sulfur electrode caused by the shuttle effect of lithium polysulfides (LiPSs) in Li-S battery, active cationic sites are introduced into COFs to obtain extended PSs adsorption region for additional PSs adsorption. The incorporation of ionic scaffolds contributes to the greater polarizability of Li-CON-TFSI compared to neutral frameworks [234]. This resulted in an enhancement of Li-Ion conduction for cationic Li-CON-TFSI COF (up to 2.09×10^{-4} S cm^{-1} at 70 °C). Liu and co-workers reported cationic COFs (S@EB-COF-PS) with sulfur content of ca. 71.7% as cathode materials for Li-S battery [235]. The specific capacity of cationic S@EB-COF-PS was 686 mA h g^{-1} at 4.0 C, much higher than that of electrically neutral S@TpPa COFs (173 mA h g^{-1}). S@EB-COF-PS still showed a specific capacity of 468 mA h g^{-1} after 300 cycles. Compared to S@TpPa, S@EB-COF-PS exhibited much higher initial specific capacities and better charge-discharge cycling performances (Fig. 9d-g). The anchoring effect of PSs is enhanced due to the introduction of active cationic sites within S@EB-COF-PS, which lowers the local electron densities and provides extra adsorption capability. The kinetic barriers of PSs polymerization and decomposition were reduced through with the use of cationic COFs, effectively suppressing the shuttle effect of LiPSs, and enhancing the performance of Li-S batteries. As such, this further inspired the research on the quantities of cationic sites introduced in COFs.

Functionalization of channel wall. Modification of channel walls by redox active groups can improve COF properties, making them suitable to be used as anode constructing materials in metal ion batteries (e.g. sodium-ion battery (SIB) and LIB) [236–238]. Chemical groups in mesoporous COFs can interact well with Na^+ ions to drive Na^+ ions into the pores of frameworks [239]. Mesoporous COFs by introducing electron-deficient substituents

bispyridine-tetrazine served as anodes for SIB and displayed high specific capacities of 340 mAh g^{-1} at 1 A g^{-1}. Electron-rich pyridine ring near the electron-deficient tetrazine center greatly improves the in-plane electronic conductivity of IISERP-COF18, and electron-deficient s-tetrazine unit can accommodate incoming electrons, and subsequently attract Na^+ in the electrolyte to maintain charge neutrality on COF pore/surface.

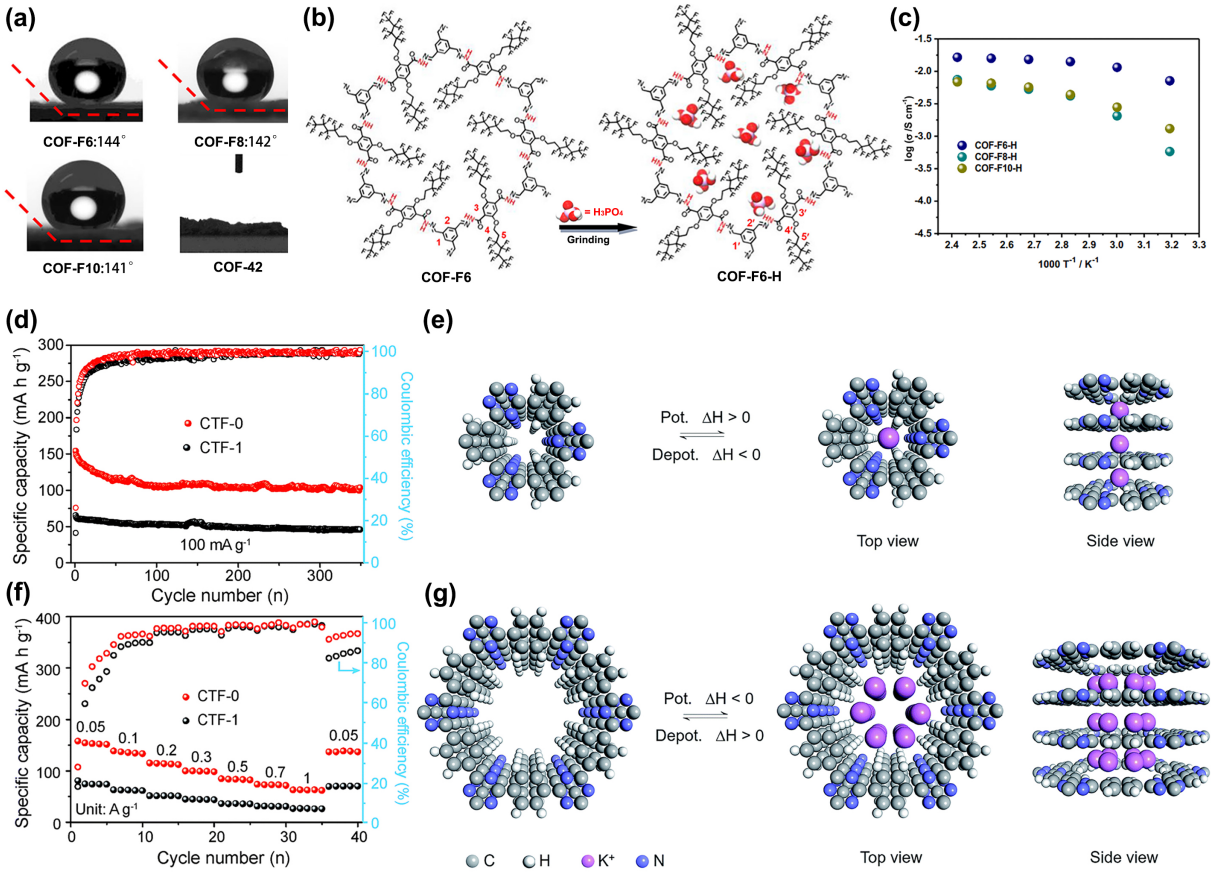

FIGURE 10. (a) Contact angles of water for COF-Fx and COF-42. (b) Scheme for the synthesis of COF-F6-H by doping H_3PO_4 into COF-F6. (c) Proton conductivities for COF-Fx-H (42 wt% H_3PO_4). (d) Cycling performance of CTF-0 and CTF-1, and (e) rate capabilities of CTF-0 and CTF1. Simulated K^+ storage mechanisms in (c) CTF-0 and (d) CTF-1. Reproduced with permission [240] and [248]. Copyright 2019, 2020, Royal Society of Chemistry.

Fuel cells convert chemical energies into electrical energies. Proton exchange membranes with excellent performances are essential in the development of fuel cells. 2D COFs have the potential to be proton transport materials, due to their uniform 1D channels, which bear

similarity to Nafion. However, parts of COF materials typically have relatively poor chemical stabilities, which restrict their applications in the acidic proton exchange condition. To overcome this disadvantage, a Perfluoroalkyl functionalized 2D COFs (COF-Fx, number of carbon atoms: x = 6, 8, or 10) were constructed to methodically investigate the effects of fluorine chain lengths on the crystalline states and proton conductivities of COFs [240]. In contrast with nonfluorous COFs (COF-42 [241]), fluorinated COFs possessed enhanced hydrophobicity (water contact angle of 144°) (Fig. 10a), and could accommodate lots of H_3PO_4 inside the superhydrophobic 1D nanochannels (Fig. 10b). After doping with H_3PO_4, the fluorinated COFs (COF-F6-H) exhibit superior proton conductivities at high temperature ($\sigma = 4.2\times10^{-2}$ S cm^{-1} at 140 °C), becoming one of the best anhydrous proton transport organic porous materials [242–246]. H_3PO_4 interacted strongly with the framework skeleton and perfluoroalkyl chains within COF channels, forming hydrogen-bonding networks. H_3PO_4 molecules within the pores were dynamic and fluid, while skeletons remained rigid, which facilitate rapid proton transports. Both H_3PO_4 loaded COF-F8-H and COF-F10-H displayed lower conductivities than COF-F6-H (Fig. 10c). This is because of their lower porosities and crystallinities resulted by their longer perfluoroalkyl side chains, which limit proton transports. Also, the proper lengths of functionalized side chains are critical to COFs' performance.

Pore size. For intercalation-type electrode materials, K^+ used has a larger ionic radius compared to Li^+ and Na^+, resulting in a greater volume change, as well as the presence of K dendrites during the charging and discharging process [247]. The pore size of the porous framework used determined the electrochemical performance and storage behavior of K ions. During the potassiation/depotassiation process, severe structural deterioration and poor cycling stability was observed on the conversion electrodes for potassium ion battery (PIB). The open and ordered channels of COFs are sufficiently large enough to accommodate potassium ions and provide convenient for ions/electrons transmission, with the formation of strong π-K^+ interaction between K^+ and π-conjugated framework skeleton. Li et al. used two CTFs with similar compositions and topology, namely CTF-0 (ultramicropores, < 7 Å) and CTF-1 (micropores, ~1.5 nm), as anode materials for PIBs, achieving favorable performance in PIBs [248]. Compared with CTF-1 (73 mAh g^{-1} at 50 mA g^{-}1), the CTF-0 (152 mAh g^{-1} at 50 mA g^{-}1) exhibited the higher charge specific capacity and reversible capacity (Fig. 10d, f).

CTF-0 with ultramicropores could only accommodate one K ions in the channel, and its depotassiation process is exothermic. Conversely, CTF-1 with larger pores was capable of holding up to six K^+ ions, and its depotassiation is endothermic (Fig. 10e, g). Therefore, the depotassiation process for CTF-0 was easier to proceed, and its ultramicropores facilitated reversible intercalation/deintercalation of K^+ ion and promoted its electrochemical performance.

Morphology. COFs with uniform morphology are more efficient in ion transport, arising from their large surface area and ordered channels. Liu et al. synthesized 3D COFs (3D-Sp-COF), with uniform hollow spherical morphology based on an Ostwald ripening strategy, for improved capacitance performance [249]. Hollow 3D-Sp-COF spheres exhibited more than 2-fold specific capacitances compared to solid 3D-Sp-COF spheres. The enhanced capacitance performance was attributed to more efficient ion transport owing to the large surface areas and hollow spherical architectures. Additionally, Wang et al. synthesized the hollow dioxin-based COF (COF-316) microflowers featuring interconnected hollow petals and ultra-thin porous walls, thereby capable of being effectively linked with conductive polypyrrole (PPy) via hydrogen bonds, and further forming unique "PPy to COF-316 to PPy" conductive networks [250]. The prepared COF-316@PPy supercapacitor displayed excellent specific capacitance (783.6 μF cm^{-2} at 3 μA cm^{-2}) and long-term cycling stability (capacitance retention of 100% after 3400 cycles) stemming from the enhanced charge transfer by hydrogen bond interaction.

To date, the studies on PIBs and SIBs are still in its infancy. Integrating coordination metals and conjugated skeleton in COFs is beneficial to specific capacitance and stability for supercapacitor due to the faster ion transport and high electrical conductivity [251]. However, parts of COFs are not suitable for coordinating with metals when they served as cathode in LIBs, which may have a serious impact on the battery. It is necessary to optimize the crystal structures, stacking density and morphology to increase the energy density of cathode materials. With regards to anode materials, one of the main challenges is the long life and high specific capacity. COFs should have good electronic/ionic conductivity, and be able to realize the reversible deintercalation/intercalation process of metal ions (such as Li^+, Na^+, and K^+).

Correlation between COFs and gas/liquid adsorption

Adsorption is a phenomenon of a single or multiple component fluid adhering to the inner and outer surfaces of porous solid through physical and/or chemical interactions. The adsorption abilities of porous solid stem from the interactions and/or bond formation (e.g., van der Waals interactions, hydrogen bonds and chemical bonds) on the absorbent surface. Chemical adsorption via chemical bonds is stronger than the physical adsorption, which rely mainly on relatively weaker van der Waals forces and hydrogen bonds. The adsorption performance is affected by the specific surface areas, porosity, pore sizes, pore environments, morphologies of the porous solid, properties of the adsorbate, etc [252–254].

Porous COFs with high crystallinity and surface areas are considered ideal materials for gas or liquid phase adsorption. COFs featuring reticular structures exhibit flexibility or breathability during adsorption. Generally, the adsorption performance of COFs is mainly dominated by the components and topologies of their frameworks [255]. The integration of alkali metals into COFs could enhance the gas adsorption capacity by improving the interaction between functional sites and gas. 3D COFs with interconnected apertures and numerous exposed functional sites would also significantly improve adsorption [256,257]. One interesting application is to use COFs for adsorption-driven heat pumps (AHPs); to use the heat generated by adsorption to achieve cooling or heating effects [258]. The equivalence of average adsorption enthalpy and evaporation enthalpy not only benefit the favorable working capacity and lower adsorption step positions, but also promote the performance of AHPs.

Pore size, shape and environment. Gas and liquid adsorption performances of COFs can be varied by tailoring the pore size, shape and environment. Utilizing different functional groups can precisely control the chemical environments of apertures to induce distinct selectivity to gases (e.g. N_2/CO_2 [259] and Xe/Kr [260]). And differing functional groups should occupy different space within the pore region to give a difference in pore size. For instance, COF-$(CF_3)_2$ modified with trifluoromethyl can adsorb fluorinated pesticides, such as trifluralin (151 mg g^{-1}) and fipronil (171 mg g^{-1}) due to strong fluorine–fluorine interactions [261]. It has been found that CO_2 adsorption sites in COFs can be formed with different

chemical substrates, including −OH, $-NO_2$ or even plain aromatic systems [262,263]. The binding sites were usually situated at small pores region, defects at the peripheral of large pores, or spaces between stacked layers. Additionally, by adding oxidizing agents and reducing agents, the hydroquinone and quinone in the framework undergo reversible conversion while the COF retains its crystallinity and porosity (Fig. 11a) [264]. This changes the pore environment, which in turn varied the selective adsorption for CO_2/N_2 mixture.

Porosity can arise from formed channels running along the stacking path in 2D layered structures. The size of these channels could be finely tuned by selecting appropriate linkers. He et al. calculated that COF-1, among a series of boron- and imine-based COFs (COF-1, -6, -8, -10, -102, MCOF-1, and COF-300, -320), had outstanding adsorption selectivity of 1.92 at 298 K and 1 bar for C_2H_6 from a C_2H_6/C_2H_4 mixture [265]. The selective C_2H_6 adsorption ability of COF-1 is attributed to the proper pore cavities (staggered interlayer structures) and unique pore environments, in which many hydrogen bonds and C–H···π interactions can be formed due to the interactions of B_3O_3 groups and benzene rings with C_2H_6. Notably, COFs composed of isomeric monomers usually have vastly different structures and performances. Distinct topological structures give various pore shapes and sizes, resulting in distinct selection and separation properties [266]. However, the designs of COFs with enhanced porosity and ultralow micropores are still very challenges.

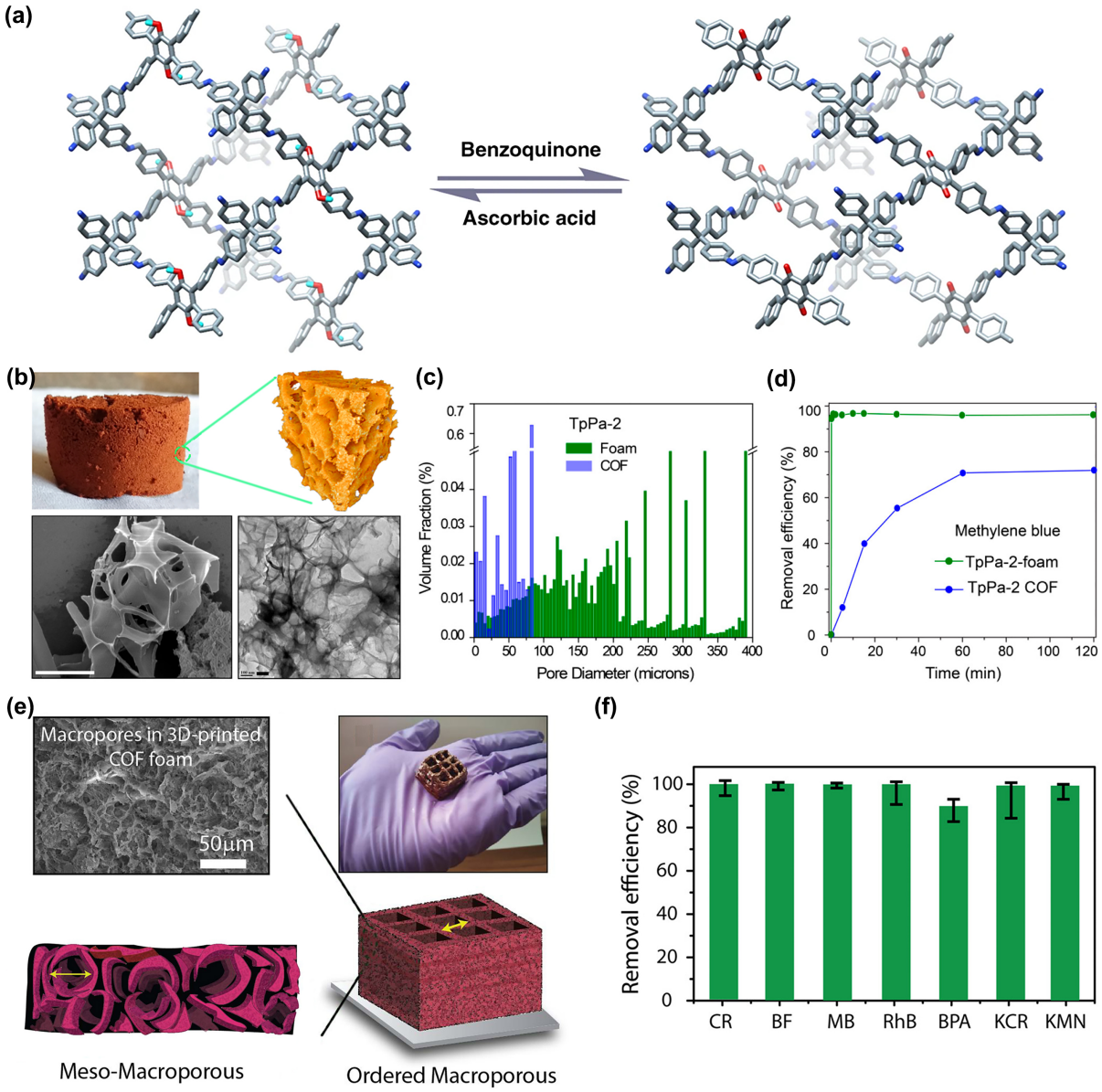

FIGURE 11. (a) Reversible crystal structure transformations between 3D-TPB-COF-HQ and 3D-TPB-COF-Q. Reproduced with permission [264]. Copyright 2020, Nature Publishing Group. (b) Structure representation of disordered macropores present in COF foam matrix. (c) Comparison of pore-size distribution between the COF–foam and COF. (d) Time-dependent removal efficiency of COF–foam and pristine COF. (e) Structure of 3D-printed TpBD foam. (f) Removal efficiency of pollutant molecules by TpBD foam. Reprodued with permission [252] and [268]. Copyright 2019, 2020, American Chemical Society.

Hierarchical porosity. It is difficult for guest molecules to reach the inner surface due to the highly stacked 2D structure and few interconnected pore channels in the powder form.

Interconnected hierarchical porous system at nano- to macro-level improve the transport and adsorption of target moiety [267]. Karak et al. manufactured COF−foams with hierarchical pores varying from μm to nm (Fig. 11b) and distribution range of 67.5% for interconnected pores (greater than 99% of the total pore volume) [252]. Compared with the COF powder (3.1-82.7 μm), pores of COF−foam have more volume fractions in the macroporous range (2.3-390 μm) (Fig. 11c). The COF−foams (TpPa-2−foam) exhibited efficient adsorption (96%-99%) for various pollutants (such as Methylene Blue (MB), Acid Fuchsin (AF) and potassium permanganate) in water within 10 s, much higher than that of TpPa-2 powder (70% within 2 h) (Fig. 11d). Various guests were also capable of diffusing quickly over the interconnected pore network of TpPa-2−foam due to the synergy of inducing ordered micropores in irregular 3D architecture. Further, 3D-printing technology was used to manufacture hierarchically porous COF-GO foams composed of ordered macropores (1.5 mm to 2 cm), disordered mesopores and macropores (50 nm to 200 μm), as well as ordered micropores (2-2.2 nm), with hierarchical pore size ranging from 10^{-9} to 10^{-3} to allow for continuous mass flow (Fig. 11e) [268]. Compared to the original COFs and powdered COF foams, COF-GO foams exhibited excellent adsorption performance and removal efficiency for different pollutants in water (Fig. 11f). The interconnected macro-, meso-, and micropores allow the access of guest molecules and provided many active sites for guests to be adsorbed onto. Also, rich and well-distributed interconnected large pores enhanced the flow of liquid, thereby realizing efficient mass transport in addition to adsorption.

Crystal size. Differing crystal sizes of COFs give distinct porosity, surface area, accessible sites, crystallinity, structure anisotropy, etc., which exert great influence on the adsorption behavior. In the N_2 and Ar adsorption, the overall absorption capacity of LZU-111 was enhanced with increasing crystal size ranging from 200 nm to 30 μm (Fig. 12a) [269]. The nano-sized LZU-111 possessed fragmentary pores with numerous defects and lacked 3D spiral channels, resulting in easy blockage of pores and low gas adsorption. Large LZU-111 crystals featured pore integrity, better anisotropy and fewer defects, thereby providing more accessible sites for gas binding (Fig. 12b). However, for flexible COF-300, the overall N_2 and Ar absorption decreased as the crystal size increased from 500 nm to 30 μm (Fig. 12c), while the adsorption capacity for CO_2 was enhanced. It is difficult to stretched or compressed large

and rigid COF-300 crystals, leading to low inert gas adsorption for N_2 and Ar. On the other hand, COF-300 has weak interactions with CO_2, which induces significant structural transformation or phase transition via a reduced energy level pathway, resulting in enhanced absorption for the gas (Fig. 12d). As such, the scalability and flexibility of COFs crystals affect unique adsorption selectivity for different substrates.

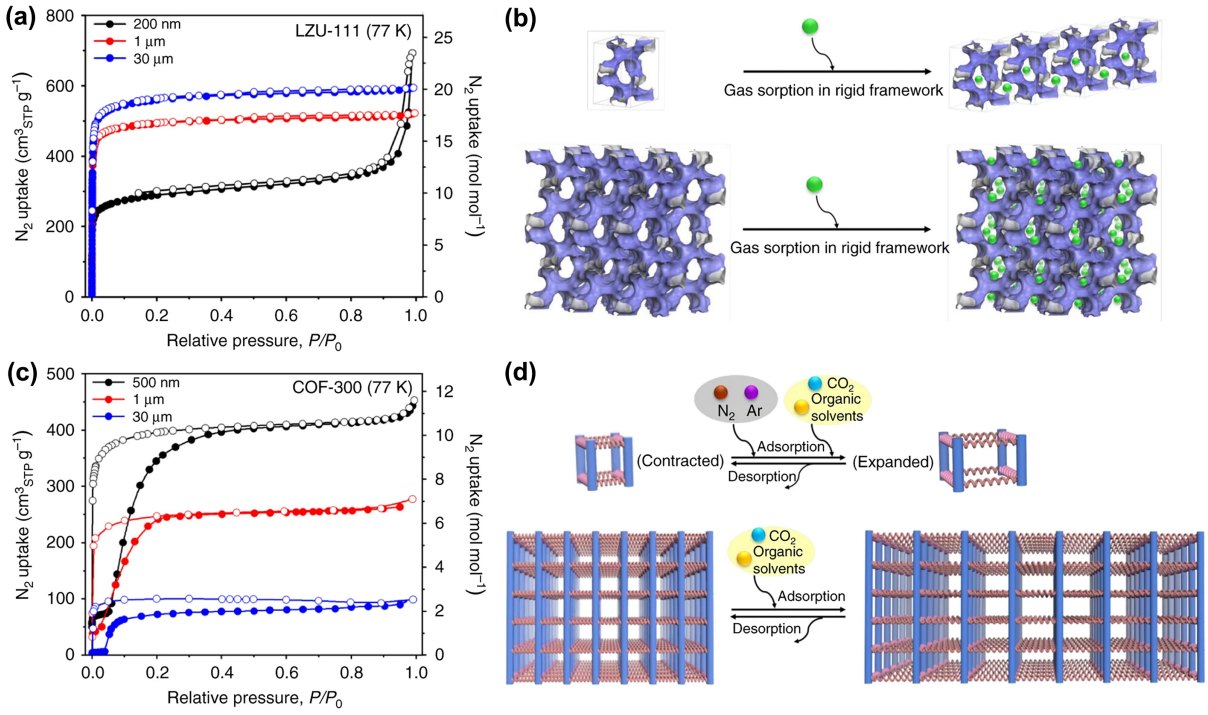

FIGURE 12. N_2 adsorption–desorption isotherms for different-sized (a) LZU-111 and (c) COF-300. Diverse crystal size effects of (b) LZU-111 and (f) COF-300. Reproduced with permission [269]. Copyright 2020, Nature Publishing Group.

Dimensionality. In general, compared with 2D COFs, 3D COFs exhibit higher adsorption capacity due to surface area along with interpenetrating networks and increased pore volumes, as well as numerous exposed openly accessible sites to permit a hierarchical alignment of nanopores [270–273]. At 273 K and 298K under 80 bar, the CO_2 adsorption capacities of 3D-PdPor-COF were 105.0 $cm^3\ g^{-1}$ and 47.7 $cm^3\ g^{-1}$ respectively, which were 3.1 and 2.4 times better than those of 2D-PdPor-COF [207]. The orderly aligned unidirectional channels of 2D COFs are not conducive for the diffusion and adsorption of guests. Transforming 2D COFs into 3D structures can effectively increasing the pore permeability and mass transfer rates of substrates through the framework, achieving rapid adsorption of guest molecules

[274]. By adopting a 3D configuration, guests were able to enter the COF skeletons via both frontal and lateral routes, interacting with the host in a more ordered and efficient manner.

Doped sites. Functional sites containing doped metal ions, such as lithium and palladium, served as adsorption sites with stronger affinity for gas, to improve gas storage capacity of COFs. Doping Li metals in nanoporous COFs gave excellent adsorption performance of COF-102 and COF-105, with CO_2 adsorption capacity of 409 and 344 mg g^{-1} respectively, at 298 K and 1 bar [275]. These were approximately four to eight times enhancement compared to COFs without ion doping, because of the strong affinity of positively charged Li ions and hydrogen. Similarly, introducing Eu(III) into COOH-3D-COF can also improve adsorption capacity (up to 211.4 mg g^{-1}) for 9,10-phenanthrenequinone (PQ), with higher PQ recovery rate (~97% vs ~60%) compared to COOH-3D-COF [276] The introduced Eu(III) interaction with the carbonyl of quinones, with the adjacent carbonyl oxygen in PQ resulting in better synergistic chelation interaction.

The introduction of fluorine atoms into the framework is also favorable to adsorption performance for organic pollutants from water. Fluorinated COF (SCF-FCOF-1) with excellent crystallinity, ultra-high porosity and surface areas (up to 2056 m^2 g^{-1}), as well as ordered channels with numerous fluorine atoms, was generated for absorption of organic dyes [253]. The adsorption capacity of SCF-FCOF-1 for malachite green, crystal violet and rhodamine B was 2701, 1106 and 1044 mg g^{-1}, respectively. The accessible and negatively charged fluorine atoms within the framework enabled electrostatic attraction with guest molecules.

Morphology. The morphologies of COFs largely affect the adsorption process. Different morphologies lead to distinct surface area, porosity and crystallinity in COFs. COFs with unique morphologies, such as hollow structure and core-shell structure, can load macromolecular enzymes to improve the stability and recyclability of expensive enzymes under harsh conditions. Typically, the core-shell COFs (Fe_3O_4@SiO_2@TpPa-Ti^{4+}) with large surface areas and pore volume, as well as doped magnetic titanium ions, were capable of quickly and selectively adsorbing phosphopeptides with high specificity (91.8%) [277]. Another COF (Fe_3O_4@COFs), with a magnetic core-shell structure, had strong adsorption capacities (82.3 to 95.4%) and recovery rates (92.9 to 109.5%) for triclosan and triclocarban,

due to the van der Waals forces, spatial embedding effect and strong π–π stacking between COFs and guests [254]. Various morphologies, including nanospheres (NS), nanorods (NR), dense microcapsules (DMS) and hollow microcapsules (HMS) COFs, were obtained, with varying adsorption performance [278]. Maximum adsorption capacities for hemoglobin of NS-, NR-, DMS-, and HMS-COF were 52.2, 166.12, 488.16, and 550.82 mg g^{-1}, respectively. The unique hollow microcapsule structure facilitates rapid and efficient adsorption, due to surface adsorption through electrostatic attraction and hydrogen bonding with the hemoglobin.

In addition, ionic COF (iCOF), fabricated by the introduction of ionic components into the framework structure, endows COFs with favorable adsorption capacity for gas molecules and metal ions [279,280]. Controlling the amount of surface charge in iCOFs may change the binding capacity of guests (such as chromium(VI)) [281]. However, the strong charge repulsion between adjacent layers of iCOF is not suitable for forming highly crystalline products, affecting the porosity, surface area, channels and exposed binding sites for molecule diffusion. Cationic knot could be utilized to modulate the planarity, and thus improving π-π stacking interactions in iCOFs [282], which partly counteracts the electrostatic repulsive force between cationic sites, and significantly reduce interlayer spacing to form crystalline iCOF. Highly crystalline iCOF with regular channels and porosity allows for sufficient molecular diffusion, resulting in faster kinetics.

Correlation between COFs and membrane/film separation

Although traditional separation techniques such as distillation, crystallization and purification have played an important role in industry, they are usually required high energy consumption. Membranes capable of selective separation for the purification and concentration of substance from different components allow for environmentally sustainable facile and efficient processing of chemicals [57]. The sieving of gases, ions, and molecules usually consider comprehensive factors such as permeability and selectivity, chemical and thermal stability, as well as cost and energy consumption. In contrast to amorphous polymers-based membranes with poorly ordered and pore channels, COFs, with uniform sized, dense and aligned pores, are more efficient selective separation membranes [51]. COF

membranes are frequently used for proton exchange in fuel cells and gas/liquid phase separation. The applications of COF membranes for reverse osmosis (RO), ultrafiltration (UF), nanofiltration (NF), etc. rely on the pore size, mechanical and chemical stability of COFs. Separation performance of COF membranes is related to hydrophilicity/hydrophobicity, proton conductivity, surface charge and membrane arrangement [51,283].

Pore size. Pore size of COF-based membrane is one of the main factors affecting the separation capability for guest molecules. COF-based membranes with different pore sizes can effectively separate substances based on size exclusion, which can be applied to different practical applications. The aperture of COF-based membranes can be tuned by symmetry, type and connectivity of the linkers, or side chain engineering and chain length modification, allowing for the separation of a variety of guest molecules with different volumes. The pore sizes of COFs decrease while the hydrophobicity of the membranes increases with increasing the length of alkyl side chains. The smaller pore size and larger hydrophobicity of COFs reduced the solvent permeance of COFs membrane (e.g. water, ethanol, methanol and hexane) while improving the selectivity for dyes (such as Rhodamine-WT, direct black, reactive black, vitamin B-12 and reactive green 19) [284,285]. Comparatively, it was demonstrated that as the length of the alkyl spacers (ethyl, butyl, hexyl) increased, anions (e.g., chloride and hydroxide ions) conductivity of their corresponding COF membranes decreases [286], due to decreasing effective pore sizes (Fig. 13a-c). Interestingly, using diethyl ether organic spacer in COF membranes could lower the resistance to anion conduction, due to the hydrophilicity and flexibility of diethyl ether spacers. Thus, anion conductivity can be improved by using a shorter and more hydrophilic spacer, via side chain engineering to tune the pore sizes and hydrophobicity/hydrophilicity of COF membranes.

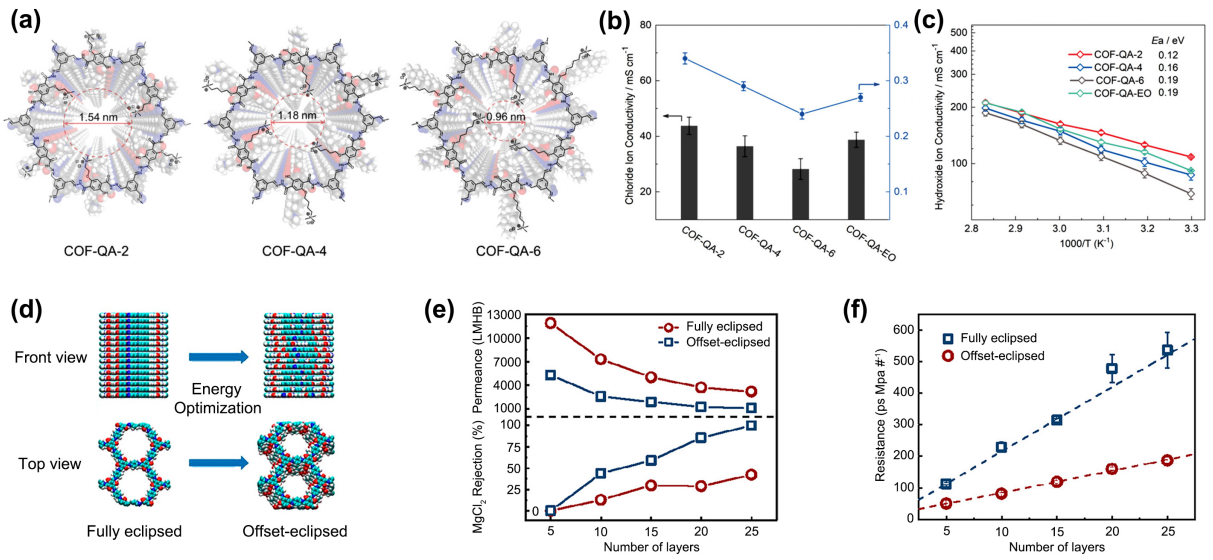

FIGURE 13. (a) Pore channels and theoretical effective pore sizes of COF-QAs with alkyl spacers. (b) Comparison of chloride ion conductivity for COF-QAs membranes at 30 ºC and 100% RH. (c) Temperature-dependent hydroxide ion conductivity of COF-QAs membranes under 100% RH. Reproduced with permission [286]. Copyright 2020, John Wiley & Sons, Inc. (d) Multilayered TpPa-1 structures before and after energy optimization. (e) Permeance and $MgCl_2$ rejection of multilayered TpPa-1 as a function of the number of layers present. (f) Resistance as a function of length for TpPa-1. Reproduced with permission [287]. Copyright 2019, American Chemical Society.

Stacking number and mode of COF layers. The stacking between COF layers (pure COFs, COFs/COFs and COFs/other materials) is important to the pore size and robustness of COF-based membranes, which gives rise to varying selectivity in gas separation, water transport and ion rejections. For the transport behaviors for water and salt ions, the TpPa-1 monolayers with pore size of ca. 1.58 nm showed higher water permeance and lower rejection to ions compared to layered TpPa-1, attributed to frictional forces arising from the electrostatic interactions between hydrophilic atoms within layered TpPa-1 and water molecules hindered water transport [287]. Compared to fully eclipsed-stacked TpPa-1, the permeance of offset-eclipsed TpPa-1 was lowered due to the reduction in pore sizes from 1.58 to 0.89 nm, while $MgCl_2$ rejection was enhanced from 42 to 100% (Fig. 13d-f). Moreover, Fan et al. prepared COF-LZU1–ACOF-1 bilayer composite membranes using COF-LZU1,

with pore size of ~1.8 nm, and ACOF-1, with pore size of ~0.94 nm [288]. Compared to pure COF-LZU1 membrane and pure ACOF-1 membrane, the COF-LZU1−ACOF-1 bilayer membrane has a much higher mixed gas separation factor of 24.2, 83.9 and 100.2 for equimolar H_2/CO_2, H_2/N_2, and H_2/CH_4 gas mixtures, respectively. The staggered pore networks, with pore sizes of 0.3-0.5 nm, formed at interconnected regions between two COFs improve the separation selectivity of COF-LZU1–ACOF-1 bilayer membrane.

In addition, by forming TpPa COF layers, with inherent nanochannels of 1.83 nm, on anodic aluminum oxide (AAO) substrates, with 20 nm pore sizes, TpPa-AAO composite membranes were fabricated for UF and NF applications [289]. Due to inter-growth of TpPa crystallites, the pore size of the staggered channels decreased, which effectively removed dye molecules larger than 1.3 nm (i.e., AF). The pore sizes of both pure COFs and overall COF-based membranes have an impact on the solvent permeances and molecular rejections of membranes. Briefly, integration of pore surface engineering and modulation of spacing between COF layers are promising research directions for the future in the field of membrane separation.

Wetting. Hydrophilicity allows water molecules to rapidly diffuse across membranes and mitigates surface fouling. Hydrogen bonds are usually formed with water molecules, which aid the transfer and flux of water molecules. The linkages (such as imine-linkage, ketoenamine-linkage and triazine-linkage) and functional groups (such as $–NH_2$, –OH, and –COOH groups and polyethylene glycol monomethyl ether) determine the hydrophilicity of the COFs-based membrane [290–292]. It has been proved that *β*-ketoamine-linked TAPA-TFP-COF and imine-linked TAPA-TFB-COF membranes possessed varying solvent permeability [293]. TAPA-TFP-COF membranes have more affinity for polar solvents, due to the relatively hydrophilic channels and polar covalent bonds of N-H and C=O on the framework structure. Conversely, TAPA-TFB-COF membrane bearing hydrophobic channels showed higher permeability to nonpolar solvents. Amine-rich COFs (SNW-1) were proposed into polyamide layer to improve its hydrophilicity [294]. Compared with pristine polyamide membrane, the water flux of SNW-1 modified membranes increased by 92%. This has huge implication for the resultant composite to be used for water desalination application. Notably, hydrophobic COFs can also be used to modify the wettability to enhance oil-water separation

performance. Decoration of isopropyl groups on COF skeletons significantly improve COF stability, due to the strong hydrophobicity of alkyl group incorporated [295]. Hydrophobic JUC-530 and JUC-531 exhibited excellent separation performance (> 99%) and separation stability (at least 30 cycles) for a wide pH range (pH 1-14) in CH_2Cl_2/water separation.

Doped functional sites. Various functional sites can be introduced into COF membranes to enhance the interaction with guest molecules. Chiral *β*-cyclodextrin (*β*-CD) was used to modify the channel of COFs [296]. The resulted COF mixed matrix membranes (MMMs) exhibit enantioselective for the transmembrane transport of L-histidine (L-His). The uniform 1D channels with *β*-CD loading in COF MMMs, which could selectively adsorb *L*-His via hydrogen bonding, was the reason for the selectivity to *L*-His. Functional sites loading in wall not only affects the pore size of the COFs, but also varied the interlayer stacking and distance. This study inspires the use of specific functional groups for modification of COF nanochannels to enable selectively separate of unique substances.

Furthermore, COFs is an ideal support for loading metal ion carriers to facilitate transport membrane. The loaded metal ion carrier and metal-binding sites located on the walls of COFs lower the resistance and facilitate the transport process inside the porous structures [297]. After loading metal ion carriers (Ag^+, Cu^{2+}, and Ni^{2+}) onto the pore walls of 2D CONs (TpHz, TpPa and TpBD), the formed transport membranes facilitated for the thiophenes removal from gasoline (Ag^+ > Cu^{2+} > Ni^{2+}) [298]. The Ag^+ loaded on the pore wall of TpHz nanosheets generates thiophene-philic microdomains with strong π-complexation with thiophene molecules. The octane sorption capacity of the facilitated transport membrane containing macropores for was enhanced, but not for thiophene, in TpPa and TpBD with different pore sizes (1.8 nm and 2.3 nm, respectively). Large pore weakens the sorption selectivity, but it also reduces the collision between the pore wall and thiophene. Therefore, increasing the pore size may enhance the adsorption capacity via sacrificing the selectivity.

Although existing COF membranes can effectively separate macromolecules, hydrated ions in solution, drugs, dyes and so on [299,300], they are not suitable for the separation of ordinary gas molecules with a kinetic diameter of 0.25-0.5nm, since the intrinsic pore diameters are usually larger (0.64-5.8 nm) [301]. However, the regular interlayer spacing of 2D COFs varying from 0.3 to 0.4 nm [302], which is comparable to the size of common gas

molecules. COF membranes should better selectivity, as well as molecular transfer rate, when straight interlayer channels are utilized for gas separation instead [303]. The straight interlayer channels in COFs provided precise size exclusion for gas separation, but vertically arranged COF membranes is difficult to manufacture and the modulation of their thickness is a challenge. Moreover, several limitations in membrane construction using COFs, such as cracks, thickness and the trade-off relationship between permeance and selectivity, still impede the progress of the field. Although a screen-printing method to directly fabricate cracks-free and thickness-tunable COF membranes has been proposed [304], there may still be obstacles in the transition of interface manufacturing technology from flat membranes to hollow fibers.

Summary and outlook

COFs have been widely used in various applications, such as catalysis, energy storage, sensing, adsorption, membrane separation, and phototherapy, due to their porous structure, with favorable surface area for rich reaction sites, large pore volumes for accessibility, high potential for guest molecules loading and tunable pore environment for mass transfer/diffusion. The nano/microstructures of COF materials serve important roles in optimizing the resultant performance. Thus, it is significant to study how to properly control and modulate the nano/microstructures of COFs. In this review, chemical and synthetic routes for conventional, novel and large-scale preparation of COFs were illustrated and correlations between structural characteristics and application performances were evaluated. Various factors were discussed, including composition, pore size, shape, pore environment, crystallinity, metal coordination, layered structures, stacking modes, dimensionality, linkage, morphology etc. Tunable structural characteristics of COF materials and their improvement in performances for various applications were analyzed. At the same time, highlighting structural-performance correlations also provide useful feedbacks on structural design to prepare unique COFs of various functions. As such, systematic understanding of structure-performance correlations guides rational design of novel COFs for the exploration of new applications and facilitates the integration of solid state physics, crystallography, organic chemistry and materials science.

The future for COFs with different structures and properties still faces several important challenges, which are summarized as follow:

(1) Mechanisms for the formation of 2D imine-linked COFs are still disputable. It was previously proposed that the crystalline networks were formed initially from amorphous polymers that underwent correction via repeated bond cleavages and formations for several days [305]. Conversely, new studies have showed that imine-linked COFs rapidly aggregate into crystalline sheets, before reorganization to form stacked structures [306]. More experiments and characterization are necessary to draw a congruent conclusion for the theory of COF formation.

(2) It is very necessary to develop a universal method that can manufacture various single-crystal COFs. More effective characterization techniques are also urgently needed.

(3) At present, it is still challenging to synthesize specific frameworks in sequence, and some problems such as framework interpenetration or polymorphism may exist through bottom-up design. High cost, low yield and complex synthesis process are also key issues. Therefore, controlling the framework growth and clean, economical, and operable synthesis methods should be developed to reduce costs and increase yields.

(4) Although many investigations have been carried out on the development of COF nanocrystals (nano-COFs), achieving high-crystallinity and suitable size are still major challenges to be overcome. These limitations impede the investigation of structure-performance relationships in their applications. Also, more efforts can be put on the construction of organic-inorganic hybrids and heterogeneous COFs.

(5) Topology of COF determines the geometry and channel size, affecting the overall lattice, stability, conjugated structure, optical band gap, and carrier migration. This important aspect is rarely investigated in relation to COF performance.

(6) Interactions of photons or electrons with mono-, multi-layer or bulk COFs are crucial for the development of porous electrode and sensor. However, there is a huge gap in current understanding for the correlation of structure-battery performance, especially how crystallinity, interlayer interaction, pore size and dimension impact eventual applications.

(7) In the field of membrane/films separation, the simultaneous need for a membrane with enhanced ion rejection and high membrane flux is proved to be difficult to resolve. It may be

achieved with insightful perspectives to fine tune the ionization, polarity and functionality of membrane fabricated. In addition, the behavior and interaction of guest molecules with surface/interface needs to be better understood.

(8) Most correlations on structure-performance are qualitatively focused. Therefore, it would be more preferable to have more quantitative studies to effectively compare results obtained.

(9) There are still rooms for understanding mechanical properties of COFs. Reducing disorders and wrinkles of COFs via tuning synthetic conditions can significantly improve mechanical properties. Thus, it is necessary to study the compressive strength, crystal size and interlayer stacking within COF structures.

(10) Except the above applications, it is promising to explore new applications, such as heat or sound insulation, sequential drug release, etc.

The crux and fundamental studies of thermodynamics, electronics, photosynthesis and theoretical models related to COFs are still under heavy and exciting development. In-depth study of COFs material about the synthesis-structure-performance relationships is expected to provide specific and systematic guidance for the translation to practically usable products under application conditions.

Declaration of Competing Interest

The authors declare that they have no known competing financial interests or personal relationships that could have appeared to influence the work reported in this paper.

Acknowledgement

H. Wang and Y. Yang contributed equally to this work. The authors gratefully acknowledge the financial support provided by the Projects of the National Nature Science Foundation of China (No. 22178091, 72088101 and 51739004). This research was also supported by the Ministry of Education Singapore under the Academic Research Funds (No. MOET2EP10120-0003).

Author Contributions

H. Wang and Y. Yang: Investigation, Writing - original draft.; H. Wang: Conceptualization, Writing - review &editing, Project administration, Supervision. X.Z Yuan: Supervision, Project administration. W. L. Teo: Writing - review & editing. Y. Wu: Writing - review & editing. Y. L. Zhao: Conceptualization, Project administration, Writing - review & editing.

References

[1] Y. Zhang, S.N. Riduan, Chem. Soc. Rev. 41 (2012) 2083–2094.

[2] A. Thomas, Angew. Chem. Int. Ed. 49 (2010) 8328–8344.

[3] J.-S.M. Lee, A.I. Cooper, Chem. Rev. 120 (2020) 2171–2214.

[4] A.B. Grommet, M. Feller, R. Klajn, Nat. Nanotechnol. 15 (2020) 256–271.

[5] H. Jiang, D. Alezi, M. Eddaoudi, Nat. Rev. Mater. 6 (2021) 466–487.

[6] S. Kandambeth, K. Dey, R. Banerjee, J. Am. Chem. Soc. 141 (2019) 1807–1822.

[7] H.M. El-Kaderi, J.R. Hunt, J.L. Mendoza-Cortés, A.P. Côté, R.E. Taylor, M. O'Keeffe, O.M. Yaghi, Science 316 (2007) 268–272.

[8] D. Xing, Y. Wang, P. Zhou, Y. Liu, Z. Wang, P. Wang, Z. Zheng, H. Cheng, Y. Dai, B. Huang, Appl. Catal. B 278 (2020) 119295.

[9] C.S. Diercks, O.M. Yaghi, Science 355 (2017) eaal1585.

[10] Y. Zhai, G. Liu, F. Jin, Y. Zhang, X. Gong, Z. Miao, J. Li, M. Zhang, Y. Cui, L. Zhang, Y. Liu, H. Zhang, Y. Zhao, Y. Zeng, Angew. Chem. Int. Ed. 58 (2019) 17679–17683.

[11] E. Hamzehpoor, A. Jonderian, E. McCalla, D.F. Perepichka, J. Am. Chem. Soc. 143 (2021) 13274–13280.

[12] X. Wang, L. Chen, S.Y. Chong, M.A. Little, Y. Wu, W.H. Zhu, R. Clowes, Y. Yan, M.A. Zwijnenburg, R.S. Sprick, A.I. Cooper, Nat. Chem. 10 (2018) 1180–1189.

[13] A.P. Coˆte´, A.I. Benin, N.W. Ockwig, M. O'Keeffe, A.J. Matzger, O.M. Yaghi, Science 310 (2005) 1166–1170.

[14] S. Wan, J. Guo, J. Kim, H. Ihee, D. Jiang, Angew. Chem. Int. Ed. 47 (2008) 8826–8830.

[15] H. Furukawa, O.M. Yaghi, J. Am. Chem. Soc. 131 (2009) 8875–8883.

[16] S.Y. Ding, J. Gao, Q. Wang, Y. Zhang, W.G. Song, C.Y. Su, W. Wang, J. Am. Chem. Soc. 133 (2011) 19816–19822.

[17] J.W. Colson, A.R. Woll, A. Mukherjee, M.P. Levendorf, E.L. Spitler, V.B. Shields, M.G. Spencer, J. Park, W.R. Dichtel, Science 332 (2011) 228-231.

[18] C.R. DeBlase, K.E. Silberstein, T.-T. Truong, H.D. Abruña, W.R. Dichtel, J. Am. Chem. Soc. 135 (2013) 16821–16824.

[19] T. Ma, E.A. Kapustin, S.X. Yin, L. Liang, Z. Zhou, J. Niu, L.-H. Li, Y. Wang, J. Su, J. Li, X. Wang, W.D. Wang, W. Wang, J. Sun, O.M. Yaghi, Science 361 (2018) 48–52.

[20] J. Tan, S. Namuangruk, W. Kong, N. Kungwan, J. Guo, C. Wang, Angew. Chem. Int. Ed. 55 (2016) 13979–13984.

[21] S.-Y. Ding, M. Dong, Y.-W. Wang, Y.-T. Chen, H.-Z. Wang, C.-Y. Su, W. Wang, J. Am. Chem. Soc. 138 (2016) 3031–3037.

[22] S. Lin, C.S. Diercks, Y.B. Zhang, N. Kornienko, E.M. Nichols, Y. Zhao, A.R. Paris, D. Kim, P. Yang, O.M. Yaghi, C.J. Chang, Science 349 (2015) 1208–1213.

[23] Q. Fang, J. Wang, S. Gu, R.B. Kaspar, Z. Zhuang, J. Zheng, H. Guo, S. Qiu, Y. Yan, J. Am. Chem. Soc. 137 (2015) 8352–8355.

[24] L. Stegbauer, K. Schwinghammer, B. V. Lotsch, Chem. Sci. 5 (2014) 2789–2793.

[25] H. Liao, H. Ding, B. Li, X. Ai, C. Wang, J. Mater. Chem. A 2 (2014) 8854–8858.

[26] H. Ma, H. Ren, S. Meng, Z. Yan, H. Zhao, F. Sun, G. Zhu, Chem. Commun. 49 (2013) 9773–9775.

[27] A.P. Côté, H.M. El-Kaderi, H. Furukawa, J.R. Hunt, O.M. Yaghi, J. Am. Chem. Soc. 129 (2007) 12914–12915.

[28] C. Zhao, H. Lyu, Z. Ji, C. Zhu, O.M. Yaghi, J. Am. Chem. Soc. 142 (2020) 14450–14454.

[29] W.K. Haug, E.R. Wolfson, B.T. Morman, C.M. Thomas, P.L. McGrier, J. Am. Chem. Soc. 142 (2020) 5521–5525.

[30] Y. Zhao, H. Liu, C. Wu, Z. Zhang, Q. Pan, F. Hu, R. Wang, P. Li, X. Huang, Z. Li, Angew. Chem. Int. Ed. 58 (2019) 5376–5381.

[31] F. Haase, P. Hirschle, R. Freund, S. Furukawa, Z. Ji, S. Wuttke, Angew. Chem. Int. Ed. 59 (2020) 22350–22370.

[32] B. Zhang, H. Mao, R. Matheu, J.A. Reimer, S.A. Alshmimri, S. Alshihri, O.M. Yaghi, J. Am. Chem. Soc. 141 (2019) 11420–11424.

[33] Y. Xie, J. Li, C. Lin, B. Gui, C. Ji, D. Yuan, J. Sun, C. Wang, J. Am. Chem. Soc. 143 (2021) 7279–7284.

[34] Y. Peng, L. Li, C. Zhu, B. Chen, M. Zhao, Z. Zhang, Z. Lai, X. Zhang, C. Tan, Y. Han, Y. Zhu, H. Zhang, J. Am. Chem. Soc. 142 (2020) 13162–13169.

[35] A. Mähringer, D.D. Medina, Nat. Chem. 12 (2020) 985–987.

[36] K. Geng, T. He, R. Liu, S. Dalapati, K.T. Tan, Z. Li, S. Tao, Y. Gong, Q. Jiang, D. Jiang, Chem. Rev. 120 (2020) 8814–8933.

[37] J.-X. Ma, J. Li, Y.-F. Chen, R. Ning, Y.-F. Ao, J.-M. Liu, J. Sun, D.-X. Wang, Q.-Q. Wang, J. Am. Chem. Soc. 141 (2019) 3843–3848.

[38] S. Chen, Y. Wu, Y. Zhang, W. Zhang, Y. Fu, W. Huang, T. Yan, H. Ma, J. Mater. Chem. A 8 (2020) 13702–13709.

[39] S. Yan, X. Guan, H. Li, D. Li, M. Xue, Y. Yan, V. Valtchev, S. Qiu, Q. Fang, J. Am. Chem. Soc. 141 (2019) 2920–2924.

[40] Z. Zhao, Y. Zheng, C. Wang, S. Zhang, J. Song, Y. Li, S. Ma, P. Cheng, Z. Zhang, Y. Chen, ACS Catal. 11 (2021) 2098–2107.

[41] M. Kou, W. Liu, Y. Wang, J. Huang, Y. Chen, Y. Zhou, Y. Chen, M. Ma, K. Lei, H. Xie, P.K. Wong, L. Ye, Appl. Catal. B 291 (2021) 120146.

[42] W. Huang, W. Luo, Y. Li, Mater. Today 40 (2020) 160–172.

[43] D.-G. Wang, T. Qiu, W. Guo, Z. Liang, H. Tabassum, D. Xia, R. Zou, Energy Environ. Sci. 14 (2021) 688–728.

[44] Y. Yang, P. Zhang, L. Hao, P. Cheng, Y. Chen, Z. Zhang, Angew. Chem. Int. Ed. 60 (2021) 21838–21845.

[45] W. Wang, V.S. Kale, Z. Cao, Y. Lei, S. Kandambeth, G. Zou, Y. Zhu, E. Abouhamad, O. Shekhah, L. Cavallo, M. Eddaoudi, H.N. Alshareef, Adv. Mater. (2021) 2103617.

[46] J.H. Park, M. Kwak, C. Hwang, K. Kang, N. Liu, J. Jang, B.A. Grzybowski, Adv. Mater. 33 (2021) 2101726.

[47] L. He, L. Chen, X. Dong, S. Zhang, M. Zhang, X. Dai, X. Liu, P. Lin, K. Li, C. Chen, T. Pan, F. Ma, J. Chen, M. Yuan, Y. Zhang, L. Chen, R. Zhou, Y. Han, Z. Chai, S. Wang, Chem 7 (2021) 699–714.

[48] Y. Zeng, R. Zou, Y. Zhao, Adv. Mater. 28 (2016) 2855–2873.

[49] P. Wang, Y. Peng, C. Zhu, R. Yao, H. Song, L. Kun, W. Yang, Angew. Chem. Int. Ed. 60 (2021) 19047–19052.

[50] Z. Kang, Y. Peng, Y. Qian, D. Yuan, M.A. Addicoat, T. Heine, Z. Hu, L. Tee, Z. Guo, D. Zhao, Chem. Mater. 28 (2016) 1277–1285.

[51] S. Yuan, X. Li, J. Zhu, G. Zhang, P. Van Puyvelde, B. Van Der Bruggen, Chem. Soc. Rev. 48 (2019) 2665–2681.

[52] F. Sheng, B. Wu, X. Li, T. Xu, M.A. Shehzad, X. Wang, L. Ge, H. Wang, T. Xu, Adv. Mater. (2021) 2104404.

[53] Z. Li, L. Sheng, H. Wang, X. Wang, M. Li, Y. Xu, H. Cui, H. Zhang, H. Liang, H. Xu, X. He, J. Am. Chem. Soc. 143 (2021) 92–96.

[54] O.M. Yaghi, ACS Cent. Sci. 5 (2019) 1295–1300.

[55] C. Gropp, T. Ma, N. Hanikel, O.M. Yaghi, Science 370 (2020) eabd6406.

[56] A.M. Evans, A. Giri, V.K. Sangwan, S. Xun, M. Bartnof, C.G. Torres-Castanedo, H.B. Balch, M.S. Rahn, N.P. Bradshaw, E. Vitaku, D.W. Burke, H. Li, M.J. Bedzyk, F. Wang, J.-L. Brédas, J.A. Malen, A.J.H. McGaughey, M.C. Hersam, W.R. Dichtel, P.E. Hopkins, Nat. Mater. 20 (2021) 1142–1148.

[57] Z. Wang, S. Zhang, Y. Chen, Z. Zhang, S. Ma, Chem. Soc. Rev. 49 (2020) 708–735.

[58] R.K. Sharma, P. Yadav, M. Yadav, R. Gupta, P. Rana, A. Srivastava, R. Zbořil, R.S. Varma, M. Antonietti, M.B. Gawande, Mater. Horizons 7 (2020) 411–454.

[59] X. Guan, F. Chen, Q. Fang, S. Qiu, Chem. Soc. Rev. 49 (2020) 1357–1384.

[60] J. Li, X. Jing, Q. Li, S. Li, X. Gao, X. Feng, B. Wang, Chem. Soc. Rev. 49 (2020) 3565–3604.

[61] Y. Li, W. Chen, G. Xing, D. Jiang, L. Chen, Chem. Soc. Rev. 49 (2020) 2852–2868.

[62] D. Rodríguez-San-Miguel, F. Zamora, Chem. Soc. Rev. 48 (2019) 4375–4386.

[63] B.J. Smith, N. Hwang, A.D. Chavez, J.L. Novotney, W.R. Dichtel, Chem. Commun. 51 (2015) 7532–7535.

[64] H. Li, A.D. Chavez, H. Li, H. Li, W.R. Dichtel, J.-L. Bredas, J. Am. Chem. Soc. 139 (2017) 16310–16318.

[65] A.M. Evans, L.R. Parent, N.C. Flanders, R.P. Bisbey, E. Vitaku, M.S. Kirschner, R.D. Schaller, L.X. Chen, N.C. Gianneschi, W.R. Dichtel, Science 361 (2018) 52–57.

[66] R.L. Li, N.C. Flanders, A.M. Evans, W. Ji, I. Castano, L.X. Chen, N.C. Gianneschi, W.R. Dichtel, Chem. Sci. 10 (2019) 3796–3801.

[67] H. Li, A.M. Evans, I. Castano, M.J. Strauss, W.R. Dichtel, J.-L. Bredas, J. Am. Chem. Soc. 142 (2020) 1367–1374.

[68] Y.-L. Zhu, H.-Y. Zhao, C.-L. Fu, Z.-W. Li, Z.-Y. Sun, Nanoscale 12 (2020) 22107–22115.

[69] T. Ma, J. Li, J. Niu, L. Zhang, A.S. Etman, C. Lin, D. Shi, P. Chen, L.-H. Li, X. Du, J. Sun, W. Wang, J. Am. Chem. Soc. 140 (2018) 6763–6766.

[70] Y. Zhu, C. Fu, Z. Li, Z. Sun, J. Phys. Chem. Lett. 11 (2020) 179–183.

[71] Y. Zhu, H. Zhao, C. Fu, Z. Li, Z. Sun, Z. Lu, J. Phys. Chem. Lett. 11 (2020) 9952–9956.

[72] M. Zhang, Y. Li, W. Yuan, X. Guo, C. Bai, Y. Zou, H. Long, Y. Qi, S. Li, G. Tao, C. Xia, L. Ma, Angew. Chem. Int. Ed. 60 (2021) 12396–12405.

[73] L. Grunenberg, G. Savasci, M.W. Terban, V. Duppel, I. Moudrakovski, M. Etter, R.E. Dinnebier, C. Ochsenfeld, B. V. Lotsch, J. Am. Chem. Soc. 143 (2021) 3430–3438.

[74] R.L. Li, A. Yang, N.C. Flanders, M.T. Yeung, D.T. Sheppard, W.R. Dichtel, J. Am. Chem. Soc. 143 (2021) 7081–7087.

[75] S. Wang, Y. Yang, H. Zhang, Z. Zhang, C. Zhang, X. Huang, D. Kozawa, P. Liu, B.-G. Li, W.-J. Wang, J. Am. Chem. Soc. 143 (2021) 5003–5010.

[76] S. Zhang, H. Miao, H.-M. Zhang, J.-H. Zhou, Q. Zhuang, Y.-J. Zeng, Z. Gao, J. Yuan, J.-K. Sun, Angew. Chem. Int. Ed. 59 (2020) 22109–22116.

[77] L. Peng, Q. Guo, C. Song, S. Ghosh, H. Xu, L. Wang, D. Hu, L. Shi, L. Zhao, Q. Li, T. Sakurai, H. Yan, S. Seki, Y. Liu, D. Wei, Nat. Commun. 12 (2021) 5077.

[78] A. Acharjya, L. Longworth-Dunbar, J. Roeser, P. Pachfule, A. Thomas, J. Am. Chem. Soc. 142 (2020) 14033–14038.

[79] J.Á. Martín-Illán, D. Rodríguez-San-Miguel, C. Franco, I. Imaz, D. Maspoch, J. Puigmartí-Luis, F. Zamora, Chem. Commun. 56 (2020) 6704–6707.

[80] P. Kuhn, M. Antonietti, A. Thomas, Angew. Chem. Int. Ed. 47 (2008) 3450–3453.

[81] J. Maschita, T. Banerjee, G. Savasci, F. Haase, C. Ochsenfeld, B. V. Lotsch, Angew. Chem. Int. Ed. 59 (2020) 15750–15758.

[82] J.I. Feldblyum, C.H. McCreery, S.C. Andrews, T. Kurosawa, E.J.G. Santos, V. Duong, L. Fang, A.L. Ayzner, Z. Bao, Chem. Commun. 51 (2015) 13894–13897.

[83] W. Dai, F. Shao, J. Szczerbiński, R. McCaffrey, R. Zenobi, Y. Jin, A.D. Schlüter, W. Zhang, Angew. Chem. Int. Ed. 55 (2016) 213–217.

[84] K. Dey, M. Pal, K.C. Rout, S. Kunjattu H, A. Das, R. Mukherjee, U.K. Kharul, R. Banerjee, J. Am. Chem. Soc. 139 (2017) 13083–13091.

[85] H.S. Sasmal, A. Halder, S.H. Kunjattu, K. Dey, A. Nadol, T.G. Ajithkumar, P. Ravindra Bedadur, R. Banerjee, J. Am. Chem. Soc. 141 (2019) 20371–20379.

[86] N.A. Khan, R. Zhang, H. Wu, J. Shen, J. Yuan, C. Fan, L. Cao, M.A. Olson, Z. Jiang, J. Am. Chem. Soc. 142 (2020) 13450–13458.

[87] M. Herder, J.-M. Lehn, J. Am. Chem. Soc. 140 (2018) 7647–7657.

[88] S. Ji, W. Cao, Y. Yu, H. Xu, Angew. Chem. Int. Ed. 53 (2014) 6781–6785.

[89] N. Giuseppone, J.-M. Lehn, Angew. Chem. Int. Ed. 45 (2006) 4619–4624.

[90] N. Hafezi, J.-M. Lehn, J. Am. Chem. Soc. 134 (2012) 12861–12868.

[91] Z. Miao, G. Liu, Y. Cui, Z. Liu, J. Li, F. Han, Y. Liu, X. Sun, X. Gong, Y. Zhai, Y. Zhao, Y. Zeng, Angew. Chem. Int. Ed. 58 (2019) 4906–4910.

[92] Z. Li, X. Ding, Y. Feng, W. Feng, B.-H. Han, Macromolecules 52 (2019) 1257–1265.

[93] L. Yang, Q. Guo, H. Kang, R. Chen, Y. Liu, D. Wei, Chem. Mater. 32 (2020) 5634–5640.

[94] M. Martínez-Abadía, C.T. Stoppiello, K. Strutynski, B. Lerma-Berlanga, C. Martí-Gastaldo, A. Saeki, M. Melle-Franco, A.N. Khlobystov, A. Mateo-Alonso, J. Am. Chem. Soc. 141 (2019) 14403–14410.

[95] G. Zhan, Z.-F. Cai, M. Martínez-Abadía, A. Mateo-Alonso, S. De Feyter, J. Am. Chem. Soc. 142 (2020) 5964–5968.

[96] G. Shi, J. Zhou, Z. Li, Y. Sun, L.N. Kantorovich, Q. Fang, F. Besenbacher, M. Yu, Angew. Chem. Int. Ed. 59 (2020) 15958–15962.

[97] T. Wang, H. Lv, J. Huang, H. Shan, L. Feng, Y. Mao, J. Wang, W. Zhang, D. Han, Q. Xu, P. Du, A. Zhao, X. Wu, S.L. Tait, J. Zhu, Nat. Commun. 10 (2019) 4122.

[98] C. Lu, Y.-P. Mo, Y. Hong, T. Chen, Z.-Y. Yang, L.-J. Wan, D. Wang, J. Am. Chem. Soc. 142 (2020) 14350–14356.

[99] Y. Liu, Y. Ma, Y. Zhao, X. Sun, F. Gandara, H. Furukawa, Z. Liu, H. Zhu, C. Zhu, K. Suenaga, P. Oleynikov, A.S. Alshammari, X. Zhang, O. Terasaki, O.M. Yaghi, Science 351 (2016) 365–369.

[100] H.-S. Xu, Y. Luo, P.Z. See, X. Li, Z. Chen, Y. Zhou, X. Zhao, K. Leng, I.-H. Park, R. Li, C. Liu, F. Chen, S. Xi, J. Sun, K.P. Loh, Angew. Chem. Int. Ed. 59 (2020) 11527–11532.

[101] A. Acharjya, P. Pachfule, J. Roeser, F.-J. Schmitt, A. Thomas, Angew. Chem. Int. Ed. 58 (2019) 14865–14870.

[102] T. Jadhav, Y. Fang, C.-H. Liu, A. Dadvand, E. Hamzehpoor, W. Patterson, A. Jonderian, R.S. Stein, D.F. Perepichka, J. Am. Chem. Soc. 142 (2020) 8862–8870.

[103] X. Guan, H. Li, Y. Ma, M. Xue, Q. Fang, Y. Yan, V. Valtchev, S. Qiu, Nat. Chem. 11 (2019) 587–594.

[104] X. Kang, X. Han, C. Yuan, C. Cheng, Y. Liu, Y. Cui, J. Am. Chem. Soc. 142 (2020) 16346–16356.

[105] E. Jin, K. Geng, K.H. Lee, W. Jiang, J. Li, Q. Jiang, S. Irle, D. Jiang, Angew. Chem. Int. Ed. 59 (2020) 12162–12169.

[106] S. Wang, Z. Zhang, H. Zhang, A.G. Rajan, N. Xu, Y. Yang, Y. Zeng, P. Liu, X. Zhang, Q. Mao, Y. He, J. Zhao, B.-G. Li, M.S. Strano, W.-J. Wang, Matter 1 (2019) 1592–1605.

[107] S. Wang, Y. Yang, P. Liu, Z. Zhang, C. Zhang, A. Chen, O.O. Ajao, B.-G. Li, P. Braunstein, W.-J. Wang, Cell Rep. Phys. Sci. 1 (2020) 100062.

[108] C. Ding, M. Breunig, J. Timm, R. Marschall, J. Senker, S. Agarwal, Adv. Funct. Mater. 31 (2021) 2106507.

[109] B.J. Smith, W.R. Dichtel, J. Am. Chem. Soc. 136 (2014) 8783–8789.

[110] H. Wang, Z. Zeng, P. Xu, L. Li, G. Zeng, R. Xiao, Z. Tang, D. Huang, L. Tang, C. Lai, D. Jiang, Y. Liu, H. Yi, L. Qin, S. Ye, X. Ren, W. Tang, Chem. Soc. Rev. 48 (2019) 488–516.

[111] K. Li, N.K. Wong, M.J. Strauss, A.M. Evans, M. Matsumoto, W.R. Dichtel, A. Adronov, J. Am. Chem. Soc. 143 (2021) 649–656.

[112] Y. Peng, Y. Huang, Y. Zhu, B. Chen, L. Wang, Z. Lai, Z. Zhang, M. Zhao, C. Tan, N. Yang, F. Shao, Y. Han, H. Zhang, J. Am. Chem. Soc. 139 (2017) 8698–8704.

[113] H. Zhang, ACS Nano 9 (2015) 9451–9469.

[114] D.N. Bunck, W.R. Dichtel, J. Am. Chem. Soc. 135 (2013) 14952–14955.

[115] D.W. Burke, C. Sun, I. Castano, N.C. Flanders, A.M. Evans, E. Vitaku, D.C. McLeod, R.H. Lambeth, L.X. Chen, N.C. Gianneschi, W.R. Dichtel, Angew. Chem. Int. Ed. 59 (2020) 5165–5171.

[116] R.J. Smith, P.J. King, M. Lotya, C. Wirtz, U. Khan, S. De, A. O'Neill, G.S. Duesberg, J.C. Grunlan, G. Moriarty, J. Chen, J. Wang, A.I. Minett, V. Nicolosi, J.N. Coleman, Adv. Mater. 23 (2011) 3944–3948.

[117] C. Zhang, D.-F. Hu, J.-W. Xu, M.-Q. Ma, H. Xing, K. Yao, J. Ji, Z.-K. Xu, ACS Nano 12 (2018) 12347–12356.

[118] G. Zhang, X. Li, Q. Liao, Y. Liu, K. Xi, W. Huang, X. Jia, Nat. Commun. 9 (2018) 2785.

[119] S.A. Ahmed, Q. Liao, Q. Shen, M.M.F. Ashraf Baig, J. Zhou, C. Shi, P. Muhammad, S. Hanif, K. Xi, X. Xia, K. Wang, Chem. Eur. J. 26 (2020) 12996–13001.

[120] H. Xu, J. Gao, D. Jiang, Nat. Chem. 7 (2015) 905–912.

[121] C. Kang, Z. Zhang, V. Wee, A.K. Usadi, C. David, L.S. Baugh, S. Wang, Y. Wang, D. Zhao, J. Am. Chem. Soc. 142 (2020) 12995–13002.

[122] A. Mal, R.K. Mishra, V.K. Praveen, M.A. Khayum, R. Banerjee, A. Ajayaghosh, Angew. Chem. Int. Ed. 57 (2018) 8443–8447.

[123] R. Kumar, K. Jalani, S.J. George, C.N.R. Rao, Chem. Mater. 29 (2017) 9751–9757.

[124] S.J. Barrow, S. Kasera, M.J. Rowland, J. del Barrio, O.A. Scherman, Chem. Rev. 115 (2015) 12320–12406.

[125] A. Mal, S. Vijayakumar, R.K. Mishra, J. Jacob, R.S. Pillai, B.S. Dileep Kumar, A. Ajayaghosh, Angew. Chem. Int. Ed. 59 (2020) 8713–8719.

[126] X. Li, H.-S. Xu, K. Leng, S.W. Chee, X. Zhao, N. Jain, H. Xu, J. Qiao, Q. Gao, I. Park, S.Y. Quek, U. Mirsaidov, K.P. Loh, Nat. Chem. 12 (2020) 1115–1122.

[127] Y. Jin, Y. Hu, W. Zhang, Nat. Rev. Chem. 1 (2017) 0056.

[128] R.-R. Liang, R.-H. A, S.-Q. Xu, Q.-Y. Qi, X. Zhao, J. Am. Chem. Soc. 142 (2020) 70–74.

[129] S. Chandra, S. Kandambeth, B.P. Biswal, B. Lukose, S.M. Kunjir, M. Chaudhary, R. Babarao, T. Heine, R. Banerjee, J. Am. Chem. Soc. 135 (2013) 17853–17861.

[130] B.P. Biswal, S. Chandra, S. Kandambeth, B. Lukose, T. Heine, R. Banerjee, J. Am. Chem. Soc. 135 (2013) 5328–5331.

[131] S. Wang, Q. Wang, P. Shao, Y. Han, X. Gao, L. Ma, S. Yuan, X. Ma, J. Zhou, X. Feng, B. Wang, J. Am. Chem. Soc. 139 (2017) 4258–4261.

[132] A.M. Pütz, M.W. Terban, S. Bette, F. Haase, R.E. Dinnebier, B. V. Lotsch, Chem. Sci. 11 (2020) 12647–12654.

[133] D.B. Shinde, H.B. Aiyappa, M. Bhadra, B.P. Biswal, P. Wadge, S. Kandambeth, B. Garai, T. Kundu, S. Kurungot, R. Banerjee, J. Mater. Chem. A 4 (2016) 2682–2690.

[134] S. Karak, S. Kandambeth, B.P. Biswal, H.S. Sasmal, S. Kumar, P. Pachfule, R. Banerjee, J. Am. Chem. Soc. 139 (2017) 1856–1862.

[135] M. Matsumoto, L. Valentino, G.M. Stiehl, H.B. Balch, A.R. Corcos, F. Wang, D.C. Ralph, B.J. Mariñas, W.R. Dichtel, Chem 4 (2018) 308–317.

[136] D. Zhu, Z. Zhang, L.B. Alemany, Y. Li, N. Nnorom, M. Barnes, S. Khalil, M.M. Rahman, P.M. Ajayan, R. Verduzco, Chem. Mater. 33 (2021) 3394–3400.

[137] M. Zhang, Q. Gao, C. Yang, L. Pang, H. Wang, H. Li, R. Li, L. Xu, Z. Xing, J. Hu, G. Wu, Ind. Eng. Chem. Res. 55 (2016) 10523–10532.

[138] S. Conrad, P. Kumar, F. Xue, L. Ren, S. Henning, C. Xiao, K.A. Mkhoyan, M. Tsapatsis, Angew. Chem. Int. Ed. 57 (2018) 13592–13597.

[139] M. Zhang, J. Chen, S. Zhang, X. Zhou, L. He, M. V Sheridan, M. Yuan, M. Zhang, L. Chen, X. Dai, F. Ma, J. Wang, J. Hu, G. Wu, X. Kong, R. Zhou, T.E. Albrecht-Schmitt, Z. Chai, S. Wang, J. Am. Chem. Soc. 142 (2020) 9169–9174.

[140] S. Lin, Y. Hou, X. Deng, H. Wang, S. Sun, X. Zhang, RSC Adv. 5 (2015) 41017–41024.

[141] X. Guo, Y. Tian, M. Zhang, Y. Li, R. Wen, X. Li, X. Li, Y. Xue, L. Ma, C. Xia, S. Li, Chem. Mater. 30 (2018) 2299–2308.

[142] Y. Zhi, P. Shao, X. Feng, H. Xia, Y. Zhang, Z. Shi, Y. Mu, X. Liu, J. Mater. Chem. A 6 (2018) 374–382.

[143] S. Kandambeth, V. Venkatesh, D.B. Shinde, S. Kumari, A. Halder, S. Verma, R. Banerjee, Nat. Commun. 6 (2015) 6786.

[144] X. Li, J. Qiao, S.W. Chee, H. Sen Xu, X. Zhao, H.S. Choi, W. Yu, S.Y. Quek, U. Mirsaidov, K.P. Loh, J. Am. Chem. Soc. 142 (2020) 4932–4943.

[145] L. Li, P. Zhang, Z. Zhang, Q. Lin, Y. Wu, A. Cheng, Y. Lin, C.M. Thompson, R.A. Smaldone, C. Ke, Angew. Chem. Int. Ed. 57 (2018) 5105–5109.

[146] M. Zhang, L. Li, Q. Lin, M. Tang, Y. Wu, C. Ke, J. Am. Chem. Soc. 141 (2019) 5154–5158.

[147] Y. Chen, Z.-L. Shi, L. Wei, B. Zhou, J. Tan, H.-L. Zhou, Y.-B. Zhang, J. Am. Chem. Soc. 141 (2019) 3298–3303.

[148] Y. Li, M. Karimi, Y.-N. Gong, N. Dai, V. Safarifard, H.-L. Jiang, Matter 4 (2021) 2230–2265.

[149] T. Banerjee, F. Haase, G. Savasci, K. Gottschling, C. Ochsenfeld, B. V. Lotsch, J. Am. Chem. Soc. 139 (2017) 16228–16234.

[150] T. Banerjee, B. V. Lotsch, Nat. Chem. 10 (2018) 1175–1177.

[151] S. Liu, T. Qian, M. Wang, H. Ji, X. Shen, C. Wang, C. Yan, Nat. Catal. 4 (2021) 322–331.

[152] T. Banerjee, K. Gottschling, G. Savasci, C. Ochsenfeld, B. V. Lotsch, ACS Energy Lett. 3 (2018) 400–409.

[153] Y. Wang, A. Vogel, M. Sachs, R.S. Sprick, L. Wilbraham, S.J.A. Moniz, R. Godin, M.A. Zwijnenburg, J.R. Durrant, A.I. Cooper, J. Tang, Nat. Energy 4 (2019) 746–760.

[154] C. Dai, B. Liu, Energy Environ. Sci. 13 (2020) 24–52.

[155] X. Cui, S. Lei, A.C. Wang, L. Gao, Q. Zhang, Y. Yang, Z. Lin, Nano Energy 70 (2020) 104525.

[156] Y. Yusran, H. Li, X. Guan, Q. Fang, S. Qiu, EnergyChem 2 (2020) 100035.

[157] H. Wang, H. Wang, Z. Wang, L. Tang, G. Zeng, P. Xu, M. Chen, T. Xiong, C. Zhou, X. Li, D. Huang, Y. Zhu, Z. Wang, J. Tang, Chem. Soc. Rev. 49 (2020) 4135–4165.

[158] S. Ghosh, A. Nakada, M.A. Springer, T. Kawaguchi, K. Suzuki, H. Kaji, I. Baburin, A. Kuc, T. Heine, R. Abe, S. Seki, J. Am. Chem. Soc. 142 (2020) 9752–9762.

[159] S. He, B. Yin, H. Niu, Y. Cai, Appl. Catal. B 239 (2018) 147–153.

[160] H. Yu, D. Wang, J. Am. Chem. Soc. 142 (2020) 11013–11021.

[161] Z. Li, T. He, Y. Gong, D. Jiang, Acc. Chem. Res. 53 (2020) 1672–1685.

[162] W. Li, X. Huang, T. Zeng, Y.A. Liu, W. Hu, H. Yang, Y. Zhang, K. Wen, Angew. Chem. Int. Ed. 60 (2021) 1869–1874.

[163] E. Jin, Z. Lan, Q. Jiang, K. Geng, G. Li, X. Wang, D. Jiang, Chem 5 (2019) 1632–1647.

[164] H. Liu, C. Li, H. Li, Y. Ren, J. Chen, J. Tang, Q. Yang, ACS Appl. Mater. Interfaces 12 (2020) 20354–20365.

[165] W. Chen, L. Wang, D. Mo, F. He, Z. Wen, X. Wu, H. Xu, L. Chen, Angew. Chem. Int. Ed. 59 (2020) 16902–16909.

[166] F. Yang, Y. Li, T. Zhang, Z. Zhao, G. Xing, L. Chen, Chem. Eur. J. 26 (2020) 4510–4514.

[167] W. Zhou, Q.-W. Deng, G.-Q. Ren, L. Sun, L. Yang, Y.-M. Li, D. Zhai, Y.-H. Zhou, W.-Q. Deng, Nat. Commun. 11 (2020) 4481.

[168] Q. Fang, S. Gu, J. Zheng, Z. Zhuang, S. Qiu, Y. Yan, Angew. Chem. Int. Ed. 53 (2014) 2878–2882.

[169] R.-R. Liang, S.-Y. Jiang, R.-H. A, X. Zhao, Chem. Soc. Rev. 49 (2020) 3920–3951.

[170] X. Zhao, P. Pachfule, S. Li, T. Langenhahn, M. Ye, C. Schlesiger, S. Praetz, J. Schmidt, A. Thomas, J. Am. Chem. Soc. 141 (2019) 6623–6630.

[171] N.C. Flanders, M.S. Kirschner, P. Kim, T.J. Fauvell, A.M. Evans, W. Helweh, A.P. Spencer, R.D. Schaller, W.R. Dichtel, L.X. Chen, J. Am. Chem. Soc. 142 (2020) 14957–14965.

[172] S. Wang, Q. Sun, W. Chen, Y. Tang, B. Aguila, Y. Pan, A. Zheng, Z. Yang, L. Wojtas, S. Ma, F.-S. Xiao, Matter 2 (2020) 416–427.

[173] H. Vardhan, A. Nafady, A.M. Al-Enizi, S. Ma, Nanoscale 11 (2019) 21679–21708.

[174] L. Ma, W.-B. Hu, B. Mei, H. Liu, B. Yuan, J. Zang, T. Chen, L. Zou, Z. Zou, B. Yang, Y. Yu, J.-Y. Ma, Z. Jiang, K. Wen, H. Yang, ACS Catal. 10 (2020) 4534–4542.

[175] J. Wang, J. Wang, S. Qi, M. Zhao, J. Phys. Chem. C 124 (2020) 17675–17683.

[176] B. Han, X. Ding, B. Yu, H. Wu, W. Zhou, W. Liu, C. Wei, B. Chen, D. Qi, H. Wang, K. Wang, Y. Chen, B. Chen, J. Jiang, J. Am. Chem. Soc. 143 (2021) 7104–7113.

[177] Z. Fu, X. Wang, A.M. Gardner, X. Wang, S.Y. Chong, G. Neri, A.J. Cowan, L. Liu, X. Li, A. Vogel, R. Clowes, M. Bilton, L. Chen, R.S. Sprick, A.I. Cooper, Chem. Sci. 11 (2020) 543–550.

[178] H. Rao, C.-H. Lim, J. Bonin, G.M. Miyake, M. Robert, J. Am. Chem. Soc. 140 (2018) 17830–17834.

[179] H. Lv, R. Sa, P. Li, D. Yuan, X. Wang, R. Wang, Sci. China Chem. 63 (2020) 1289–1294.

[180] H. Vardhan, A.M. Al-Enizi, A. Nafady, Y. Pan, Z. Yang, H.R. Gutiérrez, X. Han, S. Ma, Small 17 (2021) 2003970.

[181] R. Chen, Y. Wang, Y. Ma, A. Mal, X.-Y. Gao, L. Gao, L. Qiao, X.-B. Li, L.-Z. Wu, C. Wang, Nat. Commun. 12 (2021) 1354.

[182] M. Lu, J. Liu, Q. Li, M. Zhang, M. Liu, J.-L.L. Wang, D.-Q.Q. Yuan, Y.-Q.Q. Lan, Angew. Chem. Int. Ed. 58 (2019) 12392–12397.

[183] W. Zhong, R. Sa, L. Li, Y. He, L. Li, J. Bi, Z. Zhuang, Y. Yu, Z. Zou, J. Am. Chem. Soc. 141 (2019) 7615–7621.

[184] Y. Qian, D. Li, Y. Han, H. Jiang, J. Am. Chem. Soc. 142 (2020) 20763–20771.

[185] H.B. Aiyappa, J. Thote, D.B. Shinde, R. Banerjee, S. Kurungot, Chem. Mater. 28 (2016) 4375–4379.

[186] C. Qian, W. Zhou, J. Qiao, D. Wang, X. Li, W.L. Teo, X. Shi, H. Wu, J. Di, H. Wang, G. Liu, L. Gu, J. Liu, L. Feng, Y. Liu, S.Y. Quek, K.P. Loh, Y. Zhao, J. Am. Chem. Soc. 142 (2020) 18138–18149.

[187] L. Pan, M. Ai, C. Huang, L. Yin, X. Liu, R. Zhang, S. Wang, Z. Jiang, X. Zhang, J.-J. Zou, W. Mi, Nat. Commun. 11 (2020) 418.

[188] Y. Gong, W. Zhong, Y. Li, Y. Qiu, L. Zheng, J. Jiang, H. Jiang, J. Am. Chem. Soc. 142 (2020) 16723–16731.

[189] L. Gong, D. Zhang, Y. Shen, X. Wang, J. Zhang, X. Han, L. Zhang, Z. Xia, J. Catal. 390 (2020) 126–134.

[190] P. Pachfule, A. Acharjya, J. Roeser, T. Langenhahn, M. Schwarze, R. Schomäcker, A. Thomas, J. Schmidt, J. Am. Chem. Soc. 140 (2018) 1423–1427.

[191] Z. Li, S. Han, C. Li, P. Shao, H. Xia, H. Li, X. Chen, X. Feng, X. Liu, J. Mater. Chem. A 8 (2020) 8706–8715.

[192] S. Bi, P. Thiruvengadam, S. Wei, W. Zhang, F. Zhang, L. Gao, J. Xu, D. Wu, J. Chen, F. Zhang, J. Am. Chem. Soc. 142 (2020) 11893–11900.

[193] D. Li, C. Li, L. Zhang, H. Li, L. Zhu, D. Yang, Q. Fang, S. Qiu, X. Yao, J. Am. Chem. Soc. 142 (2020) 8104–8108.

[194] J. Xu, C. Yang, S. Bi, W. Wang, Y. He, D. Wu, Q. Liang, X. Wang, F. Zhang, Angew. Chem. Int. Ed. 59 (2020) 23845–23853.

[195] A. Nagai, X. Chen, X. Feng, X. Ding, Z. Guo, D. Jiang, Angew. Chem. Int. Ed. 52 (2013) 3770–3774.

[196] S.B. Alahakoon, S.D. Diwakara, C.M. Thompson, R.A. Smaldone, Chem. Soc. Rev. 49 (2020) 1344–1356.

[197] A. Kuc, M.A. Springer, K. Batra, R. Juarez-Mosqueda, C. Wöll, T. Heine, Adv. Funct. Mater. 30 (2020) 1908004.

[198] S. Jin, T. Sakurai, T. Kowalczyk, S. Dalapati, F. Xu, H. Wei, X. Chen, J. Gao, S. Seki, S. Irle, D. Jiang, Chem. Eur. J. 20 (2014) 14608–14613.

[199] E. Tavakoli, A. Kakekhani, S. Kaviani, P. Tan, M.M. Ghaleni, M.A. Zaeem, A.M. Rappe, S. Nejati, J. Am. Chem. Soc. 141 (2019) 19560–19564.

[200] X. Li, P. Yadav, K.P. Loh, Chem. Soc. Rev. 49 (2020) 4835–4866.

[201] W. Kong, W. Jia, R. Wang, Y. Gong, C. Wang, P. Wu, J. Guo, Chem. Commun. 55 (2019) 75–78.

[202] B.J. Smith, L.R. Parent, A.C. Overholts, P.A. Beaucage, R.P. Bisbey, A.D. Chavez, N. Hwang, C. Park, A.M. Evans, N.C. Gianneschi, W.R. Dichtel, ACS Cent. Sci. 3 (2017) 58–65.

[203] L.M. Salonen, D.D. Medina, E. Carbó-Argibay, M.G. Goesten, L. Mafra, N. Guldris, J.M. Rotter, D.G. Stroppa, C. Rodríguez-Abreu, Chem. Commun. 52 (2016) 7986–7989.

[204] A. Halder, S. Kandambeth, B.P. Biswal, G. Kaur, N.C. Roy, M. Addicoat, J.K. Salunke, S. Banerjee, K. Vanka, T. Heine, S. Verma, R. Banerjee, Angew. Chem. Int. Ed. 55 (2016) 7806–7810.

[205] Z. Chen, K. Wang, X. Hu, P. Shi, Z. Guo, H. Zhan, ACS Appl. Mater. Interfaces 13 (2021) 1145–1151.

[206] M. Zhang, Y. Li, L. Ma, X. Guo, X. Li, K. Li, X. Wang, C. Xia, S. Li, Chem. Commun. 56 (2020) 880–883.

[207] Y. Meng, Y. Luo, J.-L. Shi, H. Ding, X. Lang, W. Chen, A. Zheng, J. Sun, C. Wang, Angew. Chem. Int. Ed. 59 (2020) 3624–3629.

[208] S. Wei, F. Zhang, W. Zhang, P. Qiang, K. Yu, X. Fu, D. Wu, S. Bi, F. Zhang, J. Am. Chem. Soc. 141 (2019) 14272–14279.

[209] C. Mo, M. Yang, F. Sun, J. Jian, L. Zhong, Z. Fang, J. Feng, D. Yu, Adv. Sci. 7 (2020) 1902988.

[210] H. Wang, C. Qian, J. Liu, Y. Zeng, D. Wang, W. Zhou, L. Gu, H. Wu, G. Liu, Y. Zhao, J. Am. Chem. Soc. 142 (2020) 4862–4871.

[211] Y. Wan, L. Wang, H. Xu, X. Wu, J. Yang, J. Am. Chem. Soc. 142 (2020) 4508–4516.

[212] Q. Li, X. Lan, G. An, L. Ricardez-Sandoval, Z. Wang, G. Bai, ACS Catal. 10 (2020) 6664–6675.

[213] L. Liu, B. Zhang, X. Tan, D. Tan, X. Cheng, B. Han, J. Zhang, Chem. Commun. 56 (2020) 4567–4570.

[214] S. Kandambeth, V.S. Kale, O. Shekhah, H.N. Alshareef, M. Eddaoudi, Adv. Energy Mater. (2021) DOI: 10.1002/aenm.202100177.

[215] V. Singh, J. Kim, B. Kang, J. Moon, S. Kim, W.Y. Kim, H.R. Byon, Adv. Energy Mater. 11 (2021) 2003735.

[216] Z. Wang, Y. Yang, Z. Zhao, P. Zhang, Y. Zhang, J. Liu, S. Ma, P. Cheng, Y. Chen, Z. Zhang, Nat. Commun. 12 (2021) 1982.

[217] Y. Du, H. Yang, J.M. Whiteley, S. Wan, Y. Jin, S.-H. Lee, W. Zhang, Angew. Chem. Int. Ed. 55 (2016) 1737–1741.

[218] D. Guo, F. Ming, D.B. Shinde, L. Cao, G. Huang, C. Li, Z. Li, Y. Yuan, M.N. Hedhili, H.N. Alshareef, Z. Lai, Adv. Funct. Mater. 31 (2021) 2101194.

[219] P. Peng, L. Shi, F. Huo, S. Zhang, C. Mi, Y. Cheng, Z. Xiang, ACS Nano 13 (2019) 878–884.

[220] C. Wu, Y. Liu, H. Liu, C. Duan, Q. Pan, J. Zhu, F. Hu, X. Ma, T. Jiu, Z. Li, Y. Zhao, J. Am. Chem. Soc. 140 (2018) 10016–10024.

[221] Y. Tian, G. Zhu, Chem. Rev. 120 (2020) 8934–8986.

[222] L. Bai, Q. Gao, Y. Zhao, J. Mater. Chem. A 4 (2016) 14106–14110.

[223] Z.W. Seh, Y. Sun, Q. Zhang, Y. Cui, Chem. Soc. Rev. 45 (2016) 5605–5634.

[224] S. Royuela, J. Almarza, M.J. Mancheño, J.C. Pérez-Flores, E.G. Michel, M.M. Ramos, F. Zamora, P. Ocón, J.L. Segura, Chem. Eur. J. 25 (2019) 12394–12404.

[225] H. Shin, D. Kim, H.J. Kim, J. Kim, K. Char, C.T. Yavuz, J.W. Choi, Chem. Mater. 31 (2019) 7910–7921.

[226] S.N. Talapaneni, T.H. Hwang, S.H. Je, O. Buyukcakir, J.W. Choi, A. Coskun, Angew. Chem. Int. Ed. 55 (2016) 3106–3111.

[227] M. Zhang, X. Song, M. Yao, C. Hao, J. Qiu, J. Phys. Chem. Lett. 10 (2019) 7445–7451.

[228] J. Wan, J. Xie, X. Kong, Z. Liu, K. Liu, F. Shi, A. Pei, H. Chen, W. Chen, J. Chen, X. Zhang, L. Zong, J. Wang, L.-Q. Chen, J. Qin, Y. Cui, Nat. Nanotechnol. 14 (2019) 705–711.

[229] X. Yang, Y. Hu, N. Dunlap, X. Wang, S. Huang, Z. Su, S. Sharma, Y. Jin, F. Huang, X. Wang, S. Lee, W. Zhang, Angew. Chem. Int. Ed. 59 (2020) 20385–20389.

[230] E. Vitaku, C.N. Gannett, K.L. Carpenter, L. Shen, H.D. Abruña, W.R. Dichtel, J. Am. Chem. Soc. 142 (2020) 16–20.

[231] S. Haldar, K. Roy, R. Kushwaha, S. Ogale, R. Vaidhyanathan, Adv. Energy Mater. 9 (2019) 1902428.

[232] D. Er, L. Dong, V.B. Shenoy, J. Phys. Chem. C 120 (2016) 174–178.

[233] X. Chen, H. Zhang, C. Ci, W. Sun, Y. Wang, ACS Nano 13 (2019) 3600–3607.

[234] H. Chen, H. Tu, C. Hu, Y. Liu, D. Dong, Y. Sun, Y. Dai, S. Wang, H. Qian, Z. Lin, L. Chen, J. Am. Chem. Soc. 140 (2018) 896–899.

[235] X. Liu, H. Chen, R. Wang, S. Zang, T.C.W. Mak, Small 16 (2020) 2002932.

[236] A. Khayum M, M. Ghosh, V. Vijayakumar, A. Halder, M. Nurhuda, S. Kumar, M. Addicoat, S. Kurungot, R. Banerjee, Chem. Sci. 10 (2019) 8889–8894.

[237] S. Gu, S. Wu, L. Cao, M. Li, N. Qin, J. Zhu, Z. Wang, Y. Li, Z. Li, J. Chen, Z. Lu, J. Am. Chem. Soc. 141 (2019) 9623–9628.

[238] Z. Zhao, W. Chen, S. Impeng, M. Li, R. Wang, Y. Liu, L. Zhang, L. Dong, J. Unruangsri, C. Peng, C. Wang, S. Namuangruk, S.Y. Lee, Y. Wang, H. Lu, J. Guo, J. Mater. Chem. A 8 (2020) 3459–3467.

[239] S. Haldar, D. Kaleeswaran, D. Rase, K. Roy, S. Ogale, R. Vaidhyanathan, Nanoscale Horizons 5 (2020) 1264–1273.

[240] X. Wu, Y. Hong, B. Xu, Y. Nishiyama, W. Jiang, J. Zhu, G. Zhang, S. Kitagawa, S. Horike, J. Am. Chem. Soc. 142 (2020) 14357–14364.

[241] F.J. Uribe-Romo, C.J. Doonan, H. Furukawa, K. Oisaki, O.M. Yaghi, J. Am. Chem. Soc. 133 (2011) 11478–11481.

[242] Q. Xu, S. Tao, Q. Jiang, D. Jiang, J. Am. Chem. Soc. 140 (2018) 7429–7432.

[243] H. Li, J. Chang, S. Li, X. Guan, D. Li, C. Li, L. Tang, M. Xue, Y. Yan, V. Valtchev, S. Qiu, Q. Fang, J. Am. Chem. Soc. 141 (2019) 13324–13329.

[244] Y. Hu, N. Dunlap, S. Wan, S. Lu, S. Huang, I. Sellinger, M. Ortiz, Y. Jin, S.H. Lee, W. Zhang, J. Am. Chem. Soc. 141 (2019) 7518–7525.

[245] K. Jeong, S. Park, G.Y. Jung, S.H. Kim, Y.-H. Lee, S.K. Kwak, S.-Y. Lee, J. Am. Chem. Soc. 141 (2019) 5880–5885.

[246] Z. Xie, B. Wang, Z. Yang, X. Yang, X. Yu, G. Xing, Y. Zhang, L. Chen, Angew. Chem. Int. Ed. 58 (2019) 15742–15746.

[247] N. Wang, C. Chu, X. Xu, Y. Du, J. Yang, Z. Bai, S. Dou, Adv. Energy Mater. 8 (2018) 1801888.

[248] S.Y. Li, W.H. Li, X.L. Wu, Y. Tian, J. Yue, G. Zhu, Chem. Sci. 10 (2019) 7695–7701.

[249] Y.-Y. Liu, X.-C. Li, S. Wang, T. Cheng, H. Yang, C. Liu, Y. Gong, W.-Y. Lai, W. Huang, Nat. Commun. 11 (2020) 5561.

[250] W. Wang, W. Zhao, T. Chen, Y. Bai, H. Xu, M. Jiang, S. Liu, W. Huang, Q. Zhao, Adv. Funct. Mater. 31 (2021) 2010306.

[251] T. Li, W.-D. Da Zhang, Y. Liu, Y. Li, C. Cheng, H. Zhu, X. Yan, Z. Li, Z.-G.G. Gu, J. Mater. Chem. A 7 (2019) 19676–19681.

[252] S. Karak, K. Dey, A. Torris, A. Halder, S. Bera, F. Kanheerampockil, R. Banerjee, J. Am. Chem. Soc. 141 (2019) 7572–7581.

[253] Q. Liao, C. Ke, X. Huang, G. Zhang, Q. Zhang, Z. Zhang, Y. Zhang, Y. Liu, F. Ning, K. Xi, J. Mater. Chem. A 7 (2019) 18959–18970.

[254] Y. Li, H. Zhang, Y. Chen, L. Huang, Z. Lin, Z. Cai, ACS Appl. Mater. Interfaces 11 (2019) 22492–22500.

[255] B. Garai, D. Shetty, T. Skorjanc, F. Gándara, N. Naleem, S. Varghese, S.K. Sharma, M. Baias, R. Jagannathan, M.A. Olson, S. Kirmizialtin, A. Trabolsi, J. Am. Chem. Soc. 143 (2021) 3407–3415.

[256] Y. Wang, Y. Liu, H. Li, X. Guan, M. Xue, Y. Yan, V. Valtchev, S. Qiu, Q. Fang, J. Am. Chem. Soc. 142 (2020) 3736–3741.

[257] H. Li, J. Ding, X. Guan, F. Chen, C. Li, L. Zhu, M. Xue, D. Yuan, V. Valtchev, Y. Yan, S. Qiu, Q. Fang, J. Am. Chem. Soc. 142 (2020) 13334–13338.

[258] W. Li, X. Xia, S. Li, ACS Appl. Mater. Interfaces 12 (2020) 3265–3273.

[259] C. Gao, J. Li, S. Yin, G. Lin, T. Ma, Y. Meng, J. Sun, C. Wang, Angew. Chem. Int. Ed. 58 (2019) 9770–9775.

[260] Z. Jia, Z. Yan, J. Zhang, Y. Zou, Y. Qi, X. Li, Y. Li, X. Guo, C. Yang, L. Ma, ACS Appl. Mater. Interfaces 13 (2021) 1127–1134.

[261] Y. Zhao, Z. Sui, Z. Chang, S. Wang, Y. Liang, X. Liu, L. Feng, Q. Chen, N. Wang, J. Mater. Chem. A 8 (2020) 25156–25164.

[262] D.D. Medina, T. Sick, T. Bein, Adv. Energy Mater. 7 (2017) 1700387.

[263] K.S. Deeg, D. Damasceno Borges, D. Ongari, N. Rampal, L. Talirz, A. V. Yakutovich, J.M. Huck, B. Smit, ACS Appl. Mater. Interfaces 12 (2020) 21559–21568.

[264] C. Gao, J. Li, S. Yin, J. Sun, C. Wang, Nat. Commun. 11 (2020) 4919.

[265] C. He, Y. Wang, Y. Chen, X. Wang, J. Yang, L. Li, J. Li, ACS Appl. Mater. Interfaces 12 (2020) 52819–52825.

[266] Y. Li, L. Guo, Y. Lv, Z. Zhao, Y. Ma, W. Chen, G. Xing, D. Jiang, L. Chen, Angew. Chem. Int. Ed. 60 (2021) 5363–5369.

[267] J.Á. Martín-Illán, D. Rodríguez-San-Miguel, O. Castillo, G. Beobide, J. Perez-Carvajal, I. Imaz, D. Maspoch, F. Zamora, Angew. Chem. Int. Ed. 60 (2021) 13969–13977.

[268] A.K. Mohammed, S. Usgaonkar, F. Kanheerampockil, S. Karak, A. Halder, M. Tharkar, M. Addicoat, T.G. Ajithkumar, R. Banerjee, J. Am. Chem. Soc. 142 (2020) 8252–8261.

[269] T. Ma, L. Wei, L. Liang, S. Yin, L. Xu, J. Niu, H. Xue, X. Wang, J. Sun, Y.-B. Zhang, W. Wang, Nat. Commun. 11 (2020) 6128.

[270] Q. Zhu, X. Wang, R. Clowes, P. Cui, L. Chen, M.A. Little, A.I. Cooper, J. Am. Chem. Soc. 142 (2020) 16842–16848.

[271] G. Lin, H. Ding, R. Chen, Z. Peng, B. Wang, C. Wang, J. Am. Chem. Soc. 139 (2017) 8705–8709.

[272] Q. Lu, Y. Ma, H. Li, X. Guan, Y. Yusran, M. Xue, Q. Fang, Y. Yan, S. Qiu, V. Valtchev, Angew. Chem. Int. Ed. 57 (2018) 6042–6048.

[273] H. Ding, J. Li, G. Xie, G. Lin, R. Chen, Z. Peng, C. Yang, B. Wang, J. Sun, C. Wang, Nat. Commun. 9 (2018) 5234.

[274] X. Guo, Y. Li, M. Zhang, K. Cao, Y. Tian, Y. Qi, S. Li, K. Li, X. Yu, L. Ma, Angew. Chem. Int. Ed. 59 (2020) 22697–22705.

[275] J. Lan, D. Cao, W. Wang, B. Smit, ACS Nano 4 (2010) 4225–4237.

[276] W. Li, P. Ren, Y. Zhou, J. Feng, Z. Ma, J. Hazard. Mater. 388 (2020) 121740.

[277] F. Ding, Y. Zhao, H. Liu, W. Zhang, Analyst 145 (2020) 4341–4351.

[278] Z. Lu, Y. Liu, X. Liu, S. Lu, Y. Li, S. Yang, Y. Qin, L. Zheng, H. Zhang, J. Mater. Chem. B 7 (2019) 1469–1474.

[279] X. Zhang, W. Li, Y. Guan, B. Zhou, J. Zhang, Chem. Eur. J. 25 (2019) 6569–6574.

[280] N. Huang, P. Wang, M.A. Addicoat, T. Heine, D. Jiang, Angew. Chem. Int. Ed. 56 (2017) 4982–4986.

[281] S. Jansone-Popova, A. Moinel, J.A. Schott, S.M. Mahurin, I. Popovs, G.M. Veith, B.A. Moyer, Environ. Sci. Technol. 53 (2019) 878–883.

[282] H.-J. Da, C.-X. Yang, H.-L. Qian, X.-P. Yan, J. Mater. Chem. A 8 (2020) 12657–12664.

[283] Y. Kong, X. He, H. Wu, Y. Yang, L. Cao, R. Li, B. Shi, G. He, Y. Liu, Q. Peng, C. Fan, Z. Zhang, Z. Jiang, Angew. Chem. Int. Ed. 60 (2021) 17638–17646.

[284] A.R. Corcos, G.A. Levato, Z. Jiang, A.M. Evans, A.G. Livingston, B.J. Mariñas, W.R. Dichtel, ACS Mater. Lett. 1 (2019) 440–446.

[285] D.B. Shinde, L. Cao, A.D.D. Wonanke, X. Li, S. Kumar, X. Liu, M.N. Hedhili, A.H. Emwas, M. Addicoat, K.W. Huang, Z. Lai, Chem. Sci. 11 (2020) 5434–5440.

[286] X. He, Y. Yang, H. Wu, G. He, Z. Xu, Y. Kong, L. Cao, B. Shi, Z. Zhang, C. Tongsh, K. Jiao, K. Zhu, Z. Jiang, Adv. Mater. 32 (2020) 2001284.

[287] W. Zhou, M. Wei, X. Zhang, F. Xu, Y. Wang, ACS Appl. Mater. Interfaces 11 (2019) 16847–16854.

[288] H. Fan, A. Mundstock, A. Feldhoff, A. Knebel, J. Gu, H. Meng, J. Caro, J. Am. Chem. Soc. 140 (2018) 10094–10098.

[289] X. Shi, A. Xiao, C. Zhang, Y. Wang, J. Memb. Sci. 576 (2019) 116–122.

[290] N.A. Khan, J. Yuan, H. Wu, T. Huang, X. You, A.U. Rahman, C.S. Azad, M.A. Olson, Z. Jiang, ACS Appl. Mater. Interfaces 12 (2020) 27777–27785.

[291] H. Wang, H. Wang, H. Jiang, A. Sheng, Z. Wei, Y. Li, C. Wu, H. Li, ACS Appl. Nano Mater. 3 (2020) 9329–9339.

[292] Y. Liu, H. Wu, S. Wu, S. Song, Z. Guo, Y. Ren, R. Zhao, L. Yang, Y. Wu, Z. Jiang, J. Memb. Sci. 618 (2021) 118693.

[293] J. Liu, G. Han, D. Zhao, K. Lu, J. Gao, T.-S. Chung, Sci. Adv. 6 (2020) eabb1110.

[294] C. Wang, Z. Li, J. Chen, Z. Li, Y. Yin, L. Cao, Y. Zhong, H. Wu, J. Memb. Sci. 523 (2017) 273–281.

[295] Y. Ma, Y. Wang, H. Li, X. Guan, B. Li, M. Xue, Y. Yan, V. Valtchev, S. Qiu, Q. Fang, Angew. Chem. Int. Ed. 59 (2020) 19633–19638.

[296] C. Yuan, X. Wu, R. Gao, X. Han, Y. Liu, Y. Long, Y. Cui, J. Am. Chem. Soc. 141 (2019) 20187–20197.

[297] L. Stegbauer, M.W. Hahn, A. Jentys, G. Savasci, C. Ochsenfeld, J.A. Lercher, B. V. Lotsch, Chem. Mater. 27 (2015) 7874–7881.

[298] M. Wang, F. Pan, H. Yang, Y. Cao, H. Wang, Y. Song, Z. Lu, M. Sun, H. Wu, Z. Jiang, J. Mater. Chem. A 7 (2019) 9912–9923.

[299] H. Fan, J. Gu, H. Meng, A. Knebel, J. Caro, Angew. Chem. Int. Ed. 57 (2018) 4083–4087.

[300] Y. Kang, Y. Xia, H. Wang, X. Zhang, Adv. Funct. Mater. 29 (2019) 1902014.

[301] J. Hou, H. Zhang, G.P. Simon, H. Wang, Adv. Mater. 32 (2020) 1902009.

[302] J.L. Segura, M.J. Mancheño, F. Zamora, Chem. Soc. Rev. 45 (2016) 5635–5671.

[303] H. Fan, M. Peng, I. Strauss, A. Mundstock, H. Meng, J. Caro, J. Am. Chem. Soc. 142 (2020) 6872–6877.

[304] J. Li, H. Rong, Y. Chen, H. Zhang, T.X. Liu, Y. Yuan, X. Zou, G. Zhu, Chem. Commun. 56 (2020) 6519–6522.

[305] B.J. Smith, A.C. Overholts, N. Hwang, W.R. Dichtel, Chem. Commun. 52 (2016) 3690–3693.

[306] C. Feriante, A.M. Evans, S. Jhulki, I. Castano, M.J. Strauss, S. Barlow, W.R. Dichtel, S.R. Marder, J. Am. Chem. Soc. 142 (2020) 18637–18644.